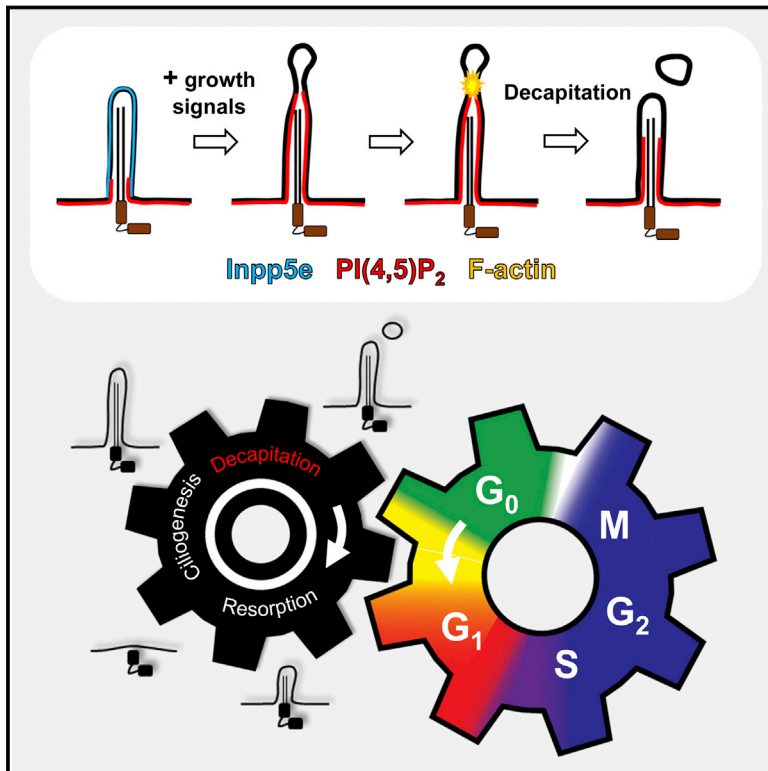# Dynamic Remodeling of Membrane Composition Drives Cell Cycle through Primary Cilia Excision

Graphical Abstract

Authors

Siew Cheng Phua, Shuhei Chiba, Masako Suzuki, ..., Jeremy F. Reiter, Koji Ikegami, Takanari Inoue

Correspondence

phua0022@e.ntu.edu.sg (S.C.P.),
kikegami@hama-med.ac.jp (K.I.),
jctinoue@jhmi.edu (T.I.)

In Brief

Release of extracellular vesicles promotes cilia disassembly and contributes to cell-cycle progression.

Highlights

- The phosphatase Inpp5e restricts actin polymerization in primary cilia

- Intraciliary PI(4,5)P$_2$ and F-actin trigger cilia decapitation

- Cilia decapitation disassembles cilia and drives cell cycle

CellPress

Dynamic Remodeling of Membrane Composition Drives Cell Cycle through Primary Cilia Excision

Siew Cheng Phua,[1,*] Shuhei Chiba,[2] Masako Suzuki,[3] Emily Su,[1] Elle C. Roberson,[4] Ganesh V. Pusapati,[6] Mitsutoshi Setou,[5] Rajat Rohatgi,[6] Jeremy F. Reiter,[4] Koji Ikegami,[5,*] and Takanari Inoue[1,7,*]

[1]Department of Cell Biology and Center for Cell Dynamics, Johns Hopkins University School of Medicine, Baltimore, MD 21205, USA
[2]Laboratory of Biological Science, Graduate School of Medicine, Osaka University, Osaka 565-0871, Japan
[3]Advanced Research Facilities and Services, Preeminent Medical Photonics Education and Research Center, Hamamatsu University School of Medicine, Hamamatsu 431-3192, Japan
[4]Department of Biochemistry and Biophysics and Cardiovascular Research Institute, University of California, San Francisco, San Francisco, CA 94158, USA
[5]Department of Cellular and Molecular Anatomy and International Mass Imaging Center, Hamamatsu University School of Medicine, Hamamatsu 431-3192, Japan
[6]Departments of Medicine and Biochemistry, Stanford University School of Medicine, Stanford, CA 94305, USA
[7]Lead Contact
*Correspondence: phua0022@e.ntu.edu.sg (S.C.P.), kikegami@hama-med.ac.jp (K.I.), jctinoue@jhmi.edu (T.I.)
http://dx.doi.org/10.1016/j.cell.2016.12.032

SUMMARY

The life cycle of a primary cilium begins in quiescence and ends prior to mitosis. In quiescent cells, the primary cilium insulates itself from contiguous dynamic membrane processes on the cell surface to function as a stable signaling apparatus. Here, we demonstrate that basal restriction of ciliary structure dynamics is established by the cilia-enriched phosphoinositide 5-phosphatase, Inpp5e. Growth induction displaces ciliary Inpp5e and accumulates phosphatidylinositol 4,5-bisphosphate in distal cilia. This change triggers otherwise-forbidden actin polymerization in primary cilia, which excises cilia tips in a process we call cilia decapitation. While cilia disassembly is traditionally thought to occur solely through resorption, we show that an acute loss of IFT-B through cilia decapitation precedes resorption. Finally, we propose that cilia decapitation induces mitogenic signaling and constitutes a molecular link between the cilia life cycle and cell-division cycle. This newly defined ciliary mechanism may find significance in cell proliferation control during normal development and cancer.

INTRODUCTION

Primary cilia function as specialized sensory antennae for cells to detect signals critical to cell proliferation and differentiation (Christensen et al., 2012; Ezratty et al., 2011; Lancaster et al., 2011; Nauli et al., 2003; Phua et al., 2015; Rohatgi et al., 2007; Singla and Reiter, 2006). Activity of cilia-dependent Gli transcription factors controls expression of cell-cycle regulators (Hui and Angers, 2011; Regl et al., 2004; Yoon et al., 2002), and mis-activation of ciliary signaling leads to cancers, including basal cell carcinoma and medulloblastoma (Han et al., 2009; Wong et al.,

2009). Hence, there is growing interest in understanding how primary cilia affect cell-cycle decisions (Basten and Giles, 2013; Kim et al., 2011; Plotnikova et al., 2008, 2009; Yeh et al., 2013). Indeed, the cilia life cycle is tightly coupled with the cell cycle; cilia assemble in non-dividing cells of G_0/G_1 phases and disassemble with cell-cycle entry (Plotnikova et al., 2009). Yet, current literature does not explain how the ciliary structure is insulated from contiguous dynamic membrane processes occurring on the cell surface, such as endo/exocytosis and membrane ruffling, to function as a stable signal transduction apparatus.

Almost all membrane processes on the cell surface depend on phosphatidylinositol 4,5-bisphosphate ($PI(4,5)P_2$), a key molecular identifier of the plasma membrane. $PI(4,5)P_2$ recruits $PI(4,5)P_2$-binding actin regulators to modulate actin polymerization at the cell cortex required to drive membrane activities on the cell surface (Saarikangas et al., 2010). Despite contiguity with plasma membrane, ciliary membrane contains $PI(4,5)P_2$ only proximally and is enriched with phosphatidylinositol 4-phosphate ($PI(4)P$) instead, creating a unique molecular identifier for ciliary membrane that distinguishes it from surrounding $PI(4,5)P_2$-enriched plasma membrane (Chávez et al., 2015; Garcia-Gonzalo et al., 2015). Such strict $PI(4)P/PI(4,5)P_2$ compartmentalization is established by Inpp5e, a cilia-enriched phosphoinositide 5-phosphatase associated with Joubert syndrome and MORM syndrome (Chávez et al., 2015; Garcia-Gonzalo et al., 2015). Loss of function of Inpp5e replenishes ciliary $PI(4,5)P_2$ and accelerates cilia disassembly depending on phosphoinositide 3-kinase, platelet-derived growth factor receptor alpha, and Aurora A kinase (AurA), implicating phosphoinositides in primary cilia stability (Bielas et al., 2009; Jacoby et al., 2009; Plotnikova et al., 2015). Moreover, primary cilia are supported by a microtubule-based axoneme and devoid of F-actin (Francis et al., 2011), unlike other F-actin-based membrane protrusions such as filopodia (Mattila and Lappalainen, 2008).

Primary cilia disassemble via gradual resorption of ciliary material into the cell body (Plotnikova et al., 2009). AurA, a master
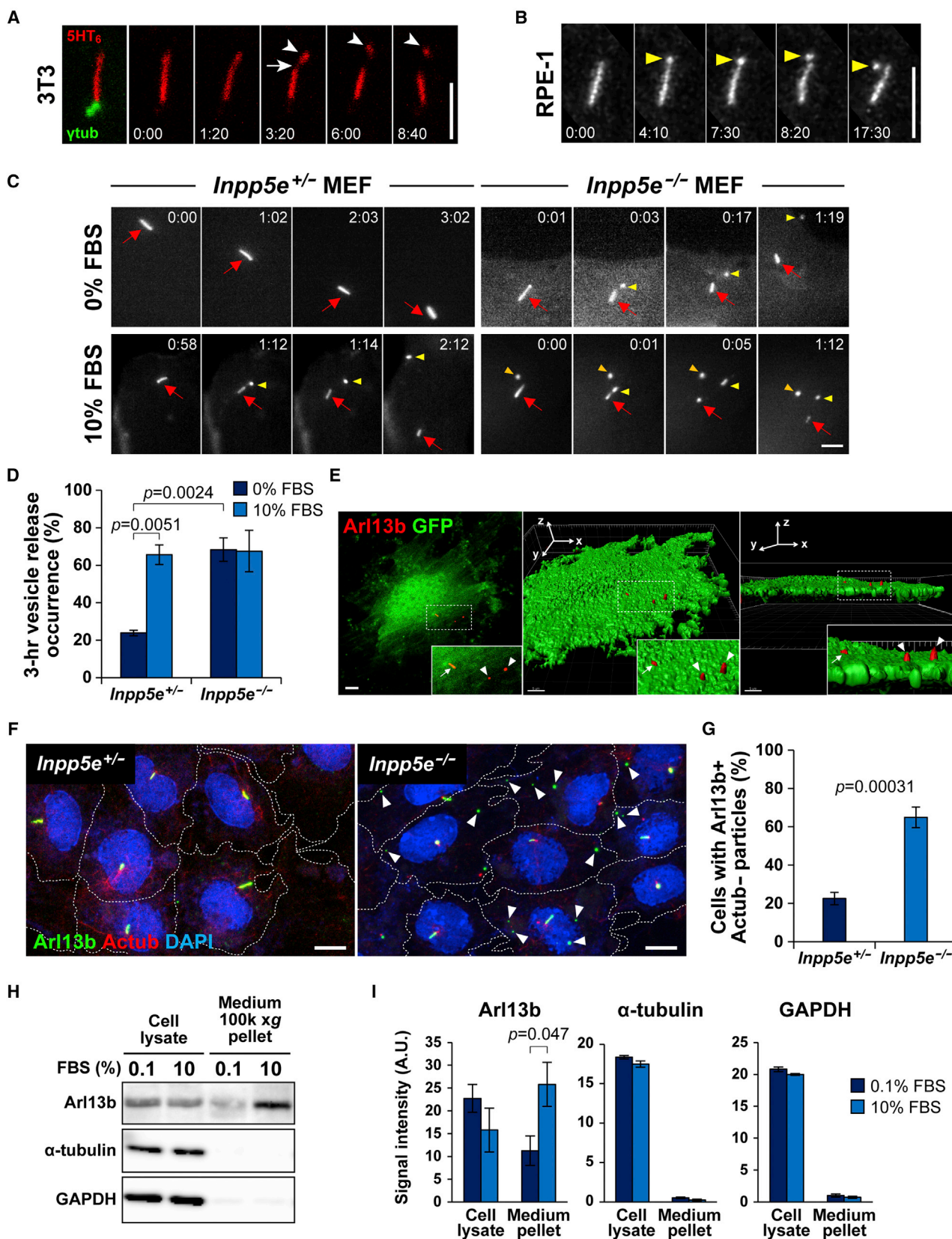
regulator of cilia disassembly, induces cilia resorption partly via histone deacetylase 6 (HDAC6)-dependent deacetylation of ciliary microtubules, which destabilizes the axoneme (Puga-cheva et al., 2007). Interestingly, *Chlamydomonas* flagella also disassemble via excision and release into the extracellular environment, in response to environmental stress such as high acidity (Pan et al., 2004). Recent reports suggest that vertebrate primary cilia could possess similar capacity in releasing vesicles into the extracellular environment (Dubreuil et al., 2007; Wood and Rosenbaum, 2015). While monitoring primary cilia of cycling kidney fibroblasts, Paridaen et al. (2013) occasionally observed release of vesicular structures from distal cilia. Active release of ciliary contents was also observed in retinal pigment epithelial cells overexpressing a CEP162 mutant (Wang et al., 2013). Furthermore, vesicular structures were closely apposed with tip-dilated primary cilia in cystic kidneys of Inpp5e mutant mice (Jacoby et al., 2009), suggesting a connection between phosphoinositides and extracellular vesicle formation. Together, this evidence supports the notion that primary cilia undergo vesicle release under specific conditions, and this process could be involved in cilia disassembly during cell-cycle entry.

RESULTS

Ciliary Vesicle Release Is Promoted by Inpp5e Loss and Growth Stimulation

We first determined factors promoting primary cilia vesicle release. Fluorescent protein (FP)-tagged ciliary membrane markers (5HT$_6$ or Arl13b) enabled live-cell visualization of ciliary vesicle release, and primary cilia were induced by culturing cells in 0%–0.1% fetal bovine serum (FBS) for 24–48 hr to attain quiescence. In NIH/3T3, hTERT RPE-1, and mIMCD-3, we occasionally observed release of ciliary vesicles from distal cilia (Figures 1A, 1B, and S1A and Movie S1). Since Inpp5e is implicated in cilia stability and extracellular vesicles (Bielas et al., 2009; Jacoby et al., 2009), we established *Inpp5e$^{+/-}$* and *Inpp5e$^{-/-}$* mouse embryonic fibroblasts (MEFs) and compared ciliary vesicle release (Garcia-Gonzalo et al., 2015). In quiescent cells, the length of *Inpp5e$^{-/-}$* cilia was shorter than *Inpp5e$^{+/-}$* cilia and displayed a higher tendency of bulging at ciliary tips (Figures S1B and S1D–S1F). The percentage of ciliation was also lower in *Inpp5e$^{-/-}$* MEFs, which displayed an accelerated cilia

disassembly rate than *Inpp5e$^{+/-}$* MEFs (Figures S1B, S1C, and S1G). Ciliary vesicle release was observed in quiescent *Inpp5e$^{+/-}$* MEFs with a low 3 hr occurrence of 23.8% ± 1.5% (mean ± SEM), while a complete loss of Inpp5e resulted in a higher 3 hr occurrence of 68.3% ± 6.3% (mean ± SEM) (Figures 1C and 1D and Movie S2). Released ciliary vesicles frequently associate with the cell surface and could be traced in fixed cell samples as Arl13b-positive and acetylated α-tubulin (Actub)-negative particles that were harbored by a higher proportion of *Inpp5e$^{-/-}$* MEFs than *Inpp5e$^{+/-}$* MEFs (Figures 1E–1G and S1H). These data demonstrate a role of Inpp5e in modulating ciliary vesicle release.

We next assessed the effect of growth stimulation on ciliary vesicle release. A 3 hr 10% FBS treatment on *Inpp5e$^{+/-}$* MEFs stimulated ciliary vesicle release in 65.5% ± 5.3% of total cells (mean ± SEM), but the same treatment on *Inpp5e$^{-/-}$* MEFs did not additionally induce a higher occurrence of ciliary vesicle release (Figures 1C and 1D and Movie S2). To further demonstrate the effect of growth signals on extracellular ciliary vesicle release, culture media conditioned for 24 hr with quiescent (0%–0.1% FBS) or growth-stimulated (10% FBS) mIMCD-3 cells were analyzed for ciliary markers (Figures S5D). Growth stimulation of mIMCD-3 resulted in significantly larger amounts of Arl13b detected in conditioned culture media, whereas extracellular levels of α-tubulin and GADPH were low and unaffected by growth stimulation (Figures 1H, 1I, S1I, and S1J). Ciliary vesicle release is thus promoted by Inpp5e loss and growth stimulation. Since this process occurs through an excision of primary cilia tips, we hereon refer to this process as cilia decapitation.

Growth-Stimulated Cilia Decapitation Entails Ciliary Inpp5e Depletion and PI(4,5)P$_2$ Re-distribution

We next investigated growth stimulation-Inpp5e interplay. A 4 hr 10% FBS stimulation to quiescent *Inpp5e$^{+/-}$* MEFs depleted endogenous Inpp5e in primary cilia (Figures 2A and 2B). To probe the functional role of Inpp5e on cilia decapitation, we targeted exogenous Inpp5e to primary cilia through fusion with a ciliary membrane marker and assessed the effect on cilia decapitation. As compared with 5HT$_6$-YFP, 5HT$_6$-YFP-Inpp5e(WT) reduced the proportion of *Inpp5e$^{+/-}$* MEFs harboring extracellular YFP-labeled ciliary vesicles over a 4 hr 10% FBS stimulation, while 5HT$_6$-YFP-Inpp5e(D477N; phosphatase-dead(PD)) did not exert similar effect (Figures S2A and S2B). In

---

Figure 1. Growth Stimulation Induces Ciliary Vesicle Release Regulated by Inpp5e

(A) Time-lapse images of a NIH/3T3 primary cilium expressing 5HT$_6$-mCherry and γtub-GFP (centrosome marker) at quiescent state. Arrow: ciliary membrane thinning prior to excision. Arrowheads: excised cilium tip.

(B) Time-lapse images of an hTERT RPE-1 primary cilium expressing Arl13b-GFP at quiescent state. Note ciliary tip bulging prior to excision (yellow arrowheads).

(C) Time-lapse images of *Inpp5e$^{+/-}$* and *Inpp5e$^{-/-}$* MEF primary cilia expressing 5HT$_6$-YFP at quiescent (0% FBS) or growth-stimulated (10% FBS) states. Red arrows:, cilia. Yellow arrows: excised cilia tips. Orange arrow: YFP+ particles present from beginning.

(D) Scoring % of cells that underwent ciliary vesicle release over 3 hr, as in (C). (n = 51, 49, 28, 34 cells from left to right; 3-5 experiments).

(E) Maximum intensity projection of Arl13b immunofluorescence and GFP in *Inpp5e$^{-/-}$* MEFs. Middle and right panels are 3D reconstructions of confocal image on left panel. Insets are magnifications of dotted regions. Arrows: cilia. Arrowheads: Arl13b+ particles residing on cell surface.

(F) Arl13b/Actub immunofluorescence and nuclear staining (DAPI) of quiescent *Inpp5e$^{+/-}$* and *Inpp5e$^{+/-}$* MEFs. Arrowheads: Arl13b+Actub− particles.

(G) Scoring % of cells with associated Arl13b+Actub− particles, as in (F). (n = 344, 376 cells from left to right; 3 experiments).

(H) Representative western blots in cell lysates and conditioned culture media pellets from mIMCD-3 cells treated with 0.1% or 10% FBS for 24 hr.

(I) Quantification of band signal intensities in (H). (n = 4 experiments for Arl13b, n = 3 experiments for α-tubulin and GAPDH).

Data are shown as mean ± SEM; Student's t tests were performed with p values indicated. Time in min:sec for (A) and (B), and hr:min for (C). Scale bars, 5 μm in (A), (B), (C), and (E) and 10 μm in (F). See also Figure S1 and Movies S1 and S2.
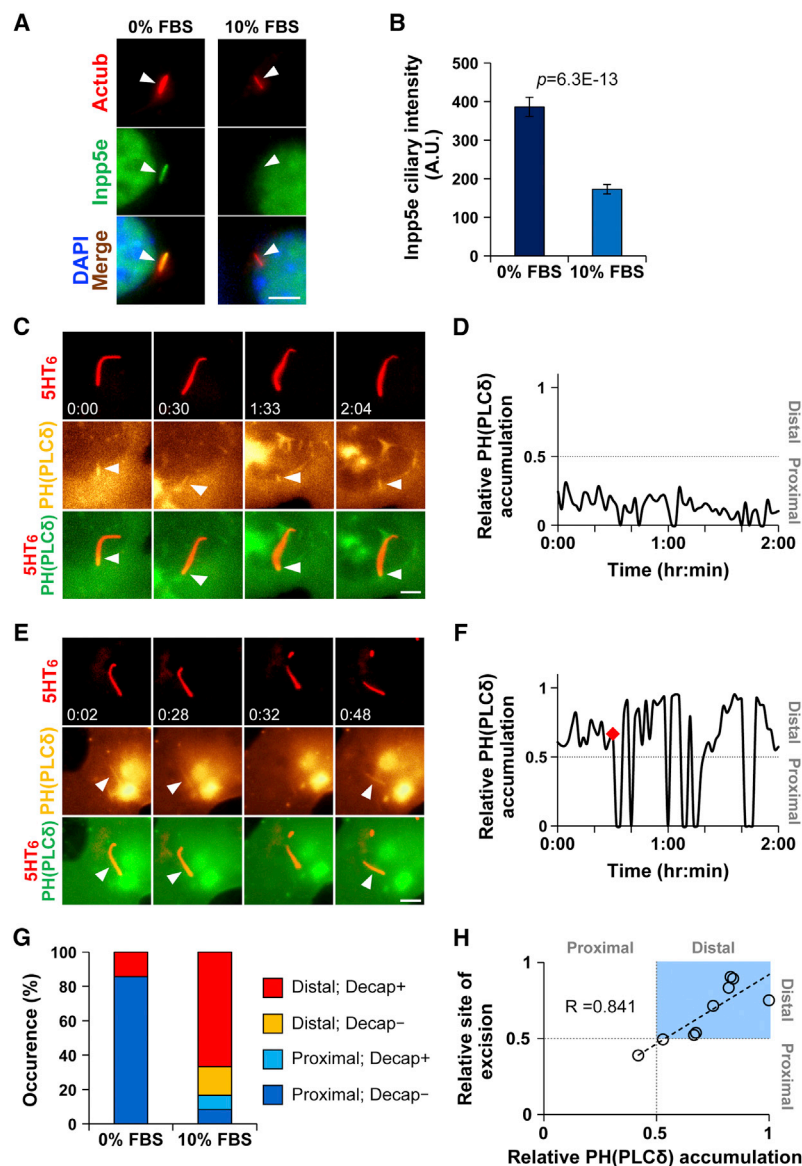
Figure 2. Growth Stimulation Regulates Ciliary Inpp5e and PI(4,5)P$_2$ Distribution

(A) Actub/Inpp5e immunofluorescence and nuclear staining (DAPI) of *Inpp5e$^{+/-}$* MEFs treated with 0% FBS or 10% FBS for 4 hr. Images of each wavelength are scaled to same intensity range. Arrowheads mark cilia positions.

(B) Inpp5e immunofluorescence signal intensity measurements in primary cilia (cilia-background), as in (A). Data shown as mean ± SEM. Student's t test was performed with p values indicated. (n = 131, 148 cells from left to right; 2 experiments.)

(C) Time-lapse images of *Inpp5e$^{+/-}$* MEF primary cilium expressing 5HT$_6$-mCeru3 and YFP-PH(PLCδ) (a PI(4,5)P$_2$ sensor) at quiescent state. Arrowheads mark PI(4,5)P$_2$ at proximal cilia.

(D) Time-lapse measurements of PH(PLCδ) proximal-distal accumulation in cilium in (C), given as relative ratio of cilium length.

(E) Time-lapse images of *Inpp5e$^{+/-}$* MEF primary cilium expressing 5HT$_6$-mCeru3 and YFP-PH(PLCδ) at 4–6 hr of 10% FBS stimulation. Arrowheads mark ciliary PI(4,5)P$_2$.

(F) Time-lapse measurements of PH(PLCδ) accumulation in cilium in (E), given as relative ratio of cilium length. Red diamond marks cilia decapitation time point.

(G) Classifying ciliary PH(PLCδ) accumulation with cilia decapitation. "Distal" or "proximal" indicates PH(PLCδ) accumulating to distal or proximal half of ciliary length. "Decap+" or "Decap−" indicates presence or absence of cilia decapitation over 2 hr imaging periods. (n = 7,12 cells from left to right; 2–3 experiments).

(H) Correlation plot of ciliary PH(PLCδ) accumulation with site of excision, each given as a relative ratio of ciliary length. In each case, the maximal ciliary PH(PLCδ) accumulation value within 10 min prior to excision is shown. Light blue box highlights distal location of ciliary PH(PLCδ) accumulation and site of cilia excision. Linear regression is drawn in dashed line, with Pearson correlation coefficient R value indicated. (n = 9 cells from 10% FBS data in [G]).

Time in hr:min for (C) and (E). Scale bars, 5 μm. See also Figure S2 and Movie S3.

quiescent *Inpp5e$^{-/-}$* MEFs, 5HT$_6$-YFP-Inpp5e(WT) also exerted a stronger repressive effect on ciliary vesicle formation than 5HT$_6$-YFP-Inpp5e(PD) (Figures S2A and S2B). Overall, these results show that Inpp5e functions as a decapitation repressor in primary cilia.

Since AurA is essential for cilia disassembly (Pugacheva et al., 2007), we examined whether inhibition of AurA and its downstream effector, HDAC6, could affect ciliary Inpp5e. AurA inhibition using alisertib (Ast) countered growth-stimulated ciliary Inpp5e depletion, whereas HDAC6 inhibition using tubacin (Tub) did not (Figures S2E and S2F). In addition, AurA was responsible for cilia decapitation, with alisertib treatment suppressing growth-stimulated ciliary vesicle release in *Inpp5e$^{+/-}$* MEFs (Figure S2G). Although HDAC6 does not regulate Inpp5e localization, tubacin treatment did exert a mild effect on ciliary vesicle release in *Inpp5e$^{+/-}$* MEFs (Figure S2G), implying that

HDAC6-mediated deacetylation of ciliary microtubules could indirectly affect cilia decapitation. Notably, neither alisertib nor tubacin inhibited ciliary vesicle release in *Inpp5e$^{-/-}$* MEFs (Figure S2G). The concomitant Inpp5e absence and AurA-independent cilia decapitation in *Inpp5e$^{-/-}$* MEFs supports that cilia tip excision requires ciliary Inpp5e depletion. Thus, growth-stimulated AurA activity drives Inpp5e depletion in primary cilia, as well as cilia decapitation.

A net Inpp5e reduction in primary cilia could result in a lower capacity to deplete PI(4,5)P$_2$. While PI(4,5)P$_2$ was confined within the proximal half of cilia in quiescent *Inpp5e$^{+/-}$* MEFs (Figures 2C, 2D, and S2H and Movie S3; Garcia-Gonzalo et al., 2015), 10% FBS stimulation led to PI(4,5)P$_2$ accumulation in distal half of *Inpp5e$^{+/-}$* cilia, concomitant with cilia decapitation (Figures 2E, 2F, and S2I–S2K and Movie S3). Decapitation primarily occurred in cilia with PI(4,5)P$_2$ accumulating to the distal half of ciliary length, and the position of cilia excision was correlated with the maximal ciliary PI(4,5)P$_2$ accumulation prior to decapitation (Figures 2G and 2H). Interestingly, cilia
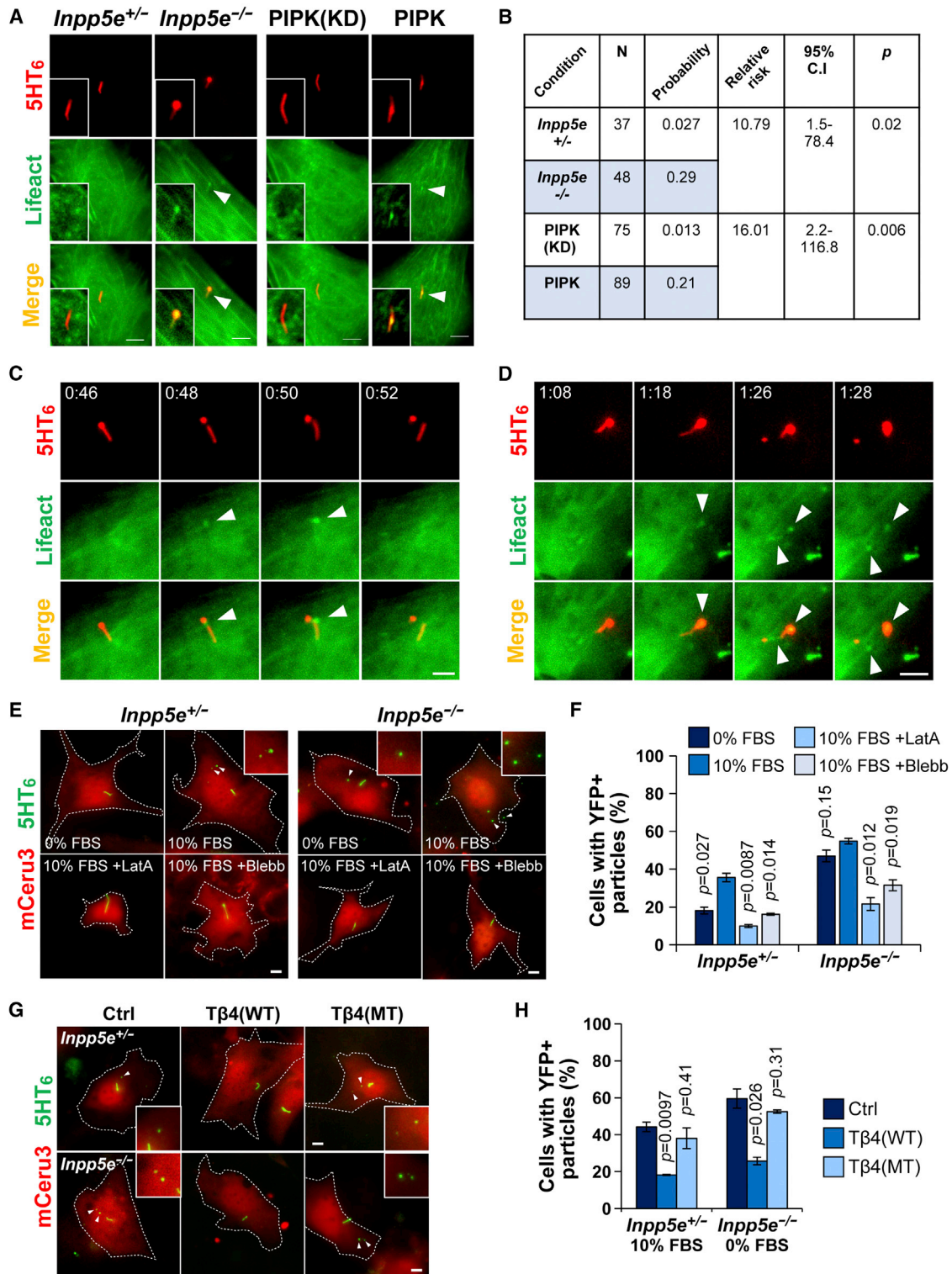
A | **B**

Table B:

Condition	N	Probability	Relative risk	95% C.I	p
Inpp5e +/-	37	0.027	10.79	1.5-78.4	0.02
Inpp5e -/-	48	0.29			
PIPK (KD)	75	0.013	16.01	2.2-116.8	0.006
PIPK	89	0.21			

Figure 3. Ciliary PI(4,5)P$_2$ Induces Intraciliary F-Actin Assembly, which Executes Cilia Decapitation

(A) Live fluorescence images of (two leftmost columns) *Inpp5e$^{+/-}$* and *Inpp5e$^{-/-}$* MEF primary cilia expressing 5HT$_6$-YFP and mCeru3-Lifeact (F-actin sensor) and (two rightmost columns) NIH/3T3 primary cilia expressing 5HT$_6$-YFP-PIPK or 5HT$_6$-YFP-PIPK(KD) and mCeru3-Lifeact at quiescent state. Insets are magnifications of respective cilia. Arrowheads mark ciliary F-actin signals.

(legend continued on next page)

decapitation was often followed by oscillations in ciliary PI(4,5)P$_2$ accumulation, which suggests bi-directional regulation between PI(4,5)P$_2$ and cilia decapitation (Figures 2E, 2F, S2J, and S2K and Movie S3). Thus, growth-stimulated PI(4,5)P$_2$ re-distribution in primary cilia could organize signaling events leading to cilia decapitation.

Ciliary PI(4,5)P$_2$ Induces F-Actin in Ciliary Lumen

Since PI(4,5)P$_2$ re-organization could affect ciliary localization of actin regulators, we inspected F-actin formation in primary cilia of $Inpp5e^{+/-}$ and $Inpp5e^{-/-}$ MEFs using mCerulean3 (mCeru3)-Lifeact biosensor. Of note, an elevated steady state of ciliary PI(4,5)P$_2$ in $Inpp5e^{-/-}$ MEFs was associated with a 10-fold increase in the probability of detecting Lifeact-positive structures in primary cilia of quiescent cells (Figures 3A and 3B). We also performed 3D super-resolution structured illumination microscopy on cells stained with phalloidin and detected similar phalloidin-labeled structures within ciliary lumen that was juxtaposed with the microtubule axoneme (Figure S3A). Direct PI(4,5)P$_2$ amplification by targeting constitutively active PI(4)P 5-kinase Iγ (PIPK) to cilia (5HT$_6$-FP-PIPK; Garcia-Gonzalo et al., 2015) was similarly associated with a higher frequency of intraciliary F-actin than cilia-targeted kinase-dead PIPK (5HT$_6$-FP-PIPK [D253A; KD]) (Figures 3A, 3B, S3B, and S3C). Therefore, ciliary PI(4,5)P$_2$ exerts direct control on intraciliary F-actin assembly. A screen for actin regulators further revealed PI(4,5)P$_2$-dependent ciliary localization of cofilin-1, fascin, and Kras small GTPase that could work together to induce actin polymerization in primary cilia (Figures S3B–S3G).

Intraciliary Actin Polymerization Is Required for Cilia Decapitation

We investigated F-actin involvement in cilia decapitation. By monitoring $Inpp5e^{+/-}$ and $Inpp5e^{-/-}$ MEFs over 2 hr periods during quiescence or between 0 and 6 hr of growth stimulation, we detected F-actin assembly at the site of cilia excision (Figures 3C, 3D, and S4A–S4I and Movie S4). These intraciliary actin polymerization events were acute and transient, occurring a few minutes prior to each decapitation event (Figures 3C, 3D, S4H, and S4I and Movie S4). Furthermore, growth-stimulated $Inpp5e^{-/-}$ MEFs tend to assemble larger intraciliary F-actin foci than quiescent $Inpp5e^{-/-}$ MEFs and growth-stimulated $Inpp5e^{+/-}$ MEFs, suggesting stronger actin polymerization that was associated with cilia excision occurring at more proximal positions (Figures S4B and S4C).

Next, we determined the essentiality of F-actin in cilia decapitation. Latrunculin A restricted growth-stimulated ciliary vesicle release in $Inpp5e^{+/-}$ and $Inpp5e^{-/-}$ MEFs, indicating that whole-cell F-actin turnover affects membrane excision in primary cilia (Figures 3E and 3F). Additionally, we devised a genetic strategy to suppress intraciliary F-actin by targeting thymosin β4 (Tβ4) to primary cilia, which sequesters G-actin from incorporation into actin filaments (Van Troys et al., 1996). As compared with 5HT$_6$-YFP, 5HT$_6$-YFP-Tβ4(WT) expression robustly suppressed ciliary vesicle formation in quiescent $Inpp5e^{-/-}$ MEFs, as well as in $Inpp5e^{+/-}$ MEFs over a 4 hr growth stimulation period (Figures 3G and 3H). In contrast, 5HT$_6$-YFP-Tβ4(KK18,19EE; actin-binding mutant MT; Van Troys et al., 1996) expression did not exert similar effect. Thus, intraciliary actin polymerization is essential for cilia decapitation, and suppression could be achieved via a genetically encoded ciliary actin inhibitor.

We then attempted to determine factors that regulate F-actin to promote ciliary membrane excision. Myosin II Inhibition with blebbistatin suppressed growth-stimulated ciliary vesicle release in $Inpp5e^{+/-}$ and $Inpp5e^{-/-}$ MEFs (Figures 3E and 3F). We also explored sorting nexin 9 (SNX9), as the molecule was detected in the proteomic profile of ciliary vesicles described in the following section. Previous reports demonstrate SNX9 as a PI(4,5)P$_2$ and PI(3,4)P$_2$ binder, which couples actin assembly with membrane remodeling at endocytic sites (Posor et al., 2013; Yarar et al., 2007). Accordingly, we observed accumulation of YFP-SNX9 in the vicinity of cilia excision site, shortly before cilia decapitation occurred in $Inpp5e^{+/-}$ MEFs (23/23; 100% of decapitation events) (Figures S4J and S4K). These results suggest a role of actomyosin contractility and SNX9-mediated actin nucleation in cilia decapitation.

Released Ciliary Vesicles Contain IFT-B and Related Cargoes

We dissected the contents of ciliary vesicles released into the extracellular milieu. Global proteomic profiling and comparative analyses were performed on culture media conditioned

---

(B) Relative risk ratio analyses on the effect of ciliary PI(4,5)P$_2$ in influencing intraciliary F-actin incidence, as in (A).

(C) Time-lapse images of a primary cilium from $Inpp5e^{+/-}$ MEFs expressing 5HT$_6$-YFP and mCeru3-Lifeact at 4–6 hr of 10% FBS stimulation. Arrowheads mark F-actin at site of cilia excision.

(D) Time-lapse images of primary cilium from $Inpp5e^{-/-}$ MEFs expressing 5HT$_6$-YFP and mCeru3-Lifeact at 0–2 hr of 10% FBS stimulation. Arrowheads mark F-actin at site of cilia excision. Note that F-actin first appeared in bulged cilia tip before expanding to proximal cilia region.

(E) Live fluorescence images of $Inpp5e^{+/-}$ and $Inpp5e^{-/-}$ MEFs expressing 5HT$_6$-YFP with mCeru3 after 3 hr in 0% FBS, 10% FBS, 10% FBS + 200 nM latrunculin A (LatA), or 10% FBS + 50 μM blebbistatin (Blebb). Arrowheads indicate cell-associated YFP+ particles that were likely vesicles released from primary cilia, and insets are respective magnified images.

(F) Quantification of percentage of cells with associated extracellular YFP+ particles, as in (E). (n = 99, 82, 70, 62, 75, 69, 73, 67 cells from left to right; 2 experiments).

(G) Live fluorescence images of $Inpp5e^{+/-}$ MEFs and $Inpp5e^{-/-}$ MEFs expressing 5HT$_6$-YFP (control), 5HT$_6$-YFP-Tβ4(WT), or 5HT$_6$-YFP-Tβ4(MT) with mCeru3, respectively, after 3 hr of 10% FBS stimulation or at quiescence (0% FBS). Arrowheads indicate cell-associated YFP+ particles, and insets are respective magnified images.

(H) Quantification of percentage of cells with associated extracellular YFP+ particles, as in (G). (n = 83, 88, 96, 69, 95, 76 cells from left to right; 2 experiments). Data shown as mean ± SEM. Student's t tests were performed with respect to (F) each 10% FBS condition and (H) each control condition, p values indicated. Time in hr:min for (C) and (D). Scale bars, 5 μm. See also Figures S3 and S4 and Movie S4.
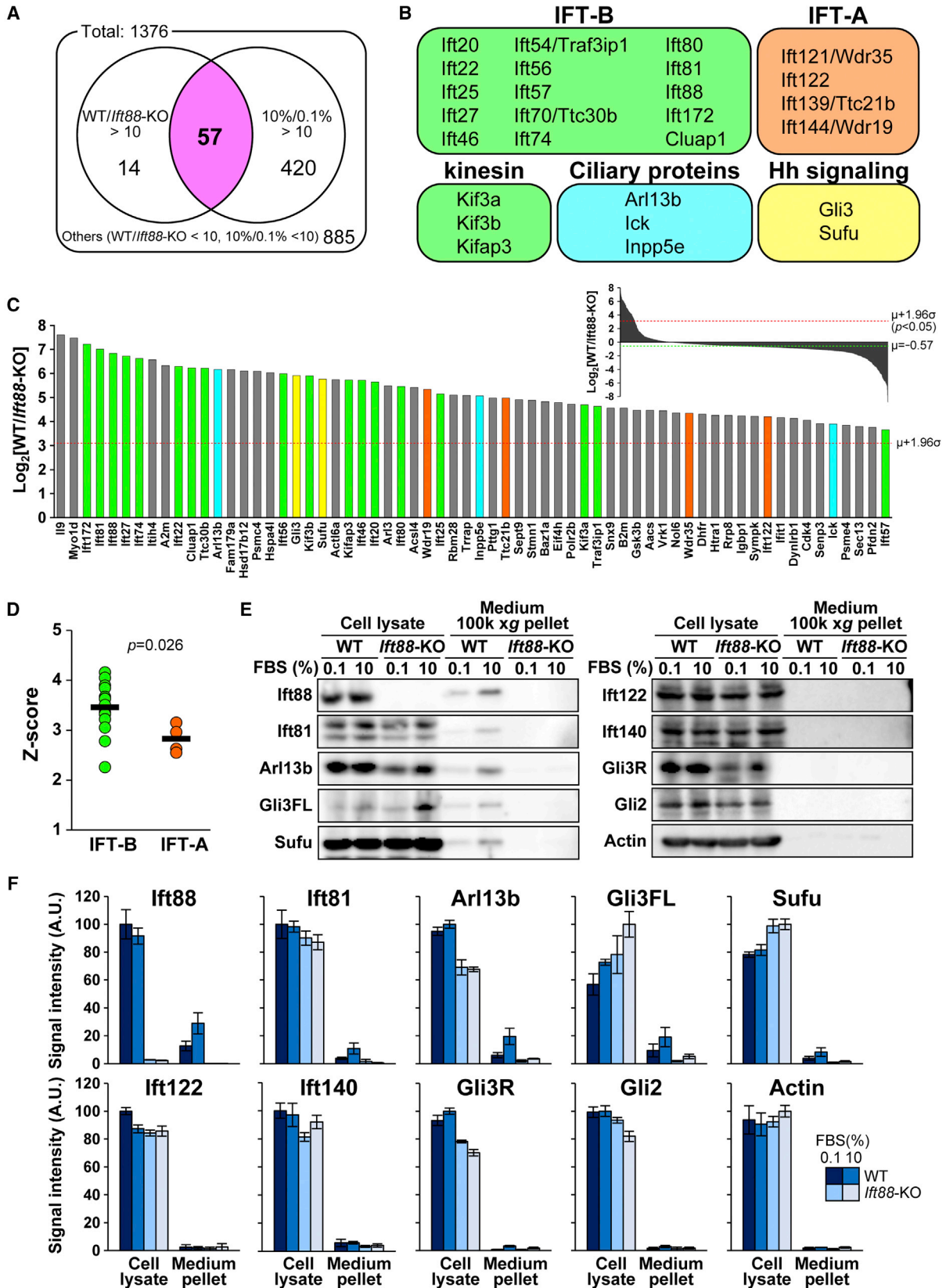
(legend on next page)

for 24 hr with quiescent (0.1% FBS) and growth-stimulated (10% FBS) wild-type (WT) or cilia-deficient *Ift88*-knockout (*Ift88*-KO) mIMCD-3 (Figures 4 and S5A–S5E), and we identified 1,376 proteins that were detected two times or more in conditioned media of at least one experiment condition (Figure 4A and Table S1). Within this list, 477 represent proteins that were extracellularly released with growth stimulation, and 71 are indicative of proteins that were extracellularly released depending on functional cilia (Figure 4A; see legend for details). A 57-protein overlap between these two categories revealed putative ciliary vesicle components, which consist of a large majority of intraflagellar transport-related proteins, a subset of ciliary proteins, and Hedgehog signaling effectors (Figure 4B and Table S1). On average, identified IFT-B components were ranked higher than IFT-A components in terms of the relative abundance between growth-stimulated WT and *Ift88*-KO mIMCD-3 culture media pellets (Figures 4C and 4D and Table S2). At the protein level, larger amounts of Arl13b, Ift88, and Ift81 (IFT-B components) were indeed detected in conditioned media pellets from growth-stimulated WT mIMCD-3 than from quiescent WT mIMCD-3 or growth-stimulated *Ift88*-KO mIMCD-3, whereas Ift122 and Ift140 (IFT-A components) were scarcely detected in conditioned media pellets from both conditions (Figures 4E and 4F). This confirms that growth-stimulated ciliary vesicle release removes IFT-B, rather than IFT-A, from primary cilia. We also validated extracellular accumulation of Sufu and full-length Gli3 (Gli3FL) in conditioned media pellets of growth-stimulated WT mIMCD-3, while Gli2 and a truncated form of Gli3 (Gli3R) were hardly detected (Figures 4E and 4F).

We proceeded to understand the mechanism for relative IFT-B enrichment in released ciliary vesicles. In quiescent cells, Ift140(IFT-A) and Ift81(IFT-B) were detected along ciliary shafts of *Inpp5e^{+/−}* and *Inpp5e^{−/−}* MEFs, with *Inpp5e^{−/−}* primary cilia harboring high enrichment of Ift140 as previously reported (Figures S5F and S5G) (Garcia-Gonzalo et al., 2015). Interestingly, a 4 hr 10% FBS stimulation led to increased ciliary Ift81 in *Inpp5e^{+/−}* and *Inpp5e^{−/−}* MEFs, while ciliary Ift140 underwent reduction in both cell types (Figures S5F and S5G). In a mIMCD-3 cell line with endogenous Ift81 tagged with yellow Nano-lantern (YNL) (Figures S5H–S5J), Ift81-YNL signals were detected throughout the ciliary shaft at quiescence, with stronger accumulation in proximal cilia (Figure S5K). A 4 hr growth stimulation not only elevated the overall Ift81-YNL in primary cilia but also slightly shifted Ift81-YNL distribution toward the distal cilia (Figures S5K–S5O). Thus, an IFT-B increase with a complementary IFT-A decrease could potentially account for the selective release of IFT-B from primary cilia upon ciliary vesicle release.

Cilia Decapitation Is Required for Cilia Disassembly

Cilia decapitation culminates in an acute loss of ciliary proteins that may compromise cilia stability. Likewise, Inpp5e loss triggers accelerated cilia instability upon growth stimulation (Figure S1G) (Bielas et al., 2009; Jacoby et al., 2009). We therefore investigated the functional consequences of decapitation in *Inpp5e^{+/−}* and *Inpp5e^{−/−}* MEF ciliary resorption. In growth-stimulated *Inpp5e^{+/−}* MEFs expressing 5HT6-YFP, the lengths of intact primary cilia were maintained (Decap− in 10% FBS; Figures 5A and 5B), while decapitated cilia underwent significant resorption within 3 hr post-decapitation (Decap+ in 10% FBS; Figures 5A and 5B). Consistently, growth-stimulated *Inpp5e^{+/−}* primary cilia inhibited for decapitation via 5HT6-YFP-Tβ4(WT) expression were also suppressed for resorption (Decap− in 10% FBS Tβ4(WT); Figures 5A and 5B). Thus, decapitation is necessary for cilia resorption induced by growth stimulation. In Inpp5e absence, growth-stimulated cilia decapitation in *Inpp5e^{−/−}* MEFs was accompanied with a greater extent of cilia resorption as compared with *Inpp5e^{+/−}* counterpart (Decap+ in 10% FBS; Figures 5A and 5C). Cilia decapitation in quiescent *Inpp5e^{−/−}* MEFs was also sufficient to activate cilia resorption within 3 hr post-decapitation, albeit to a smaller extent than in growth stimulated events (Decap+ in 0% FBS; Figures 5A and 5C). Thus, cilia resorption post-decapitation was amplified in the absence of Inpp5e.

We further probed the role of decapitation on the extent of ciliation in *Inpp5e^{+/−}* and *Inpp5e^{−/−}* MEFs expressing 5HT6-YFP, 5HT6-YFP-Tβ4(WT) and 5HT6-YFP-Tβ4(MT) at 0, 6, and 20 hr of 10% FBS stimulation. While a similar proportion of cells were ciliated at 0 hr across all three conditions, a larger proportion of 5HT6-YFP-Tβ4(WT)-expressing cells harbored primary cilia at 6 and 20 hr of growth stimulation (Figures 5D–5G). Thus, ciliary actin inhibition suppressed cilia decapitation that was required for cilia disassembly. Moreover, the observed role of 5HT6–YFP-Inpp5e(WT) in suppressing growth-stimulated

Figure 4. Global Proteomic Profiling of Conditioned Culture Media Reveals Growth-Stimulated Extracellular Release of IFT-B Dependent on Primary Cilia

(A) Venn diagram classification of proteins detected in conditioned culture media under indicated conditions, with a threshold of false discovery rate = 0.01. "10%/0.1% >10": 477 proteins with mass spectrometry signal areas ≥ 10-fold higher in 10% FBS condition than in 0.1% FBS condition, in WT mIMCD-3 (growth stimulation-dependent). "WT/*Ift88*KO >10": 71 proteins with mass spectrometry signal areas ≥ 10-fold higher in WT mIMCD-3 than *Ift88*-KO mIMCD-3, in 10% FBS condition (cilia dependent). There is a 57-protein (purple) overlap, i.e., both cilia and growth stimulation dependent.

(B) Classification of ciliary proteins among the 57 proteins highlighted in (A).

(C) Comparative analyses of proteins extracellularly released in cilia-dependent manner (WT/*Ift88*KO). Mass spectrometry signal area ratios for respective proteins are represented as logarithm to the base 2 (log2) and ranked in descending order of *Z* scores. Only top 1.2% of proteins with *Z* scores higher than 2.25 are shown. The mean (μ) log2 ratios of area values is −0.57, and SD (σ) is 1.87. Color coding as in (B).

(D) *Z* score comparison between IFT-B and IFT-A components identified from proteomic analysis, as in (C). Ift88 is excluded from IFT-B group, since a high WT/*Ift88*KO ratio would occur with *Ift88*-KO. Bars indicate mean of *Z* scores. A Mann-Whitney U-test was performed with p values indicated.

(E) Representative western blot analyses in total cell lysates and conditioned culture media pellets.

(F) Quantification of respective band signal intensities in (E). Data shown as mean ± SEM (n = 3 experiments).
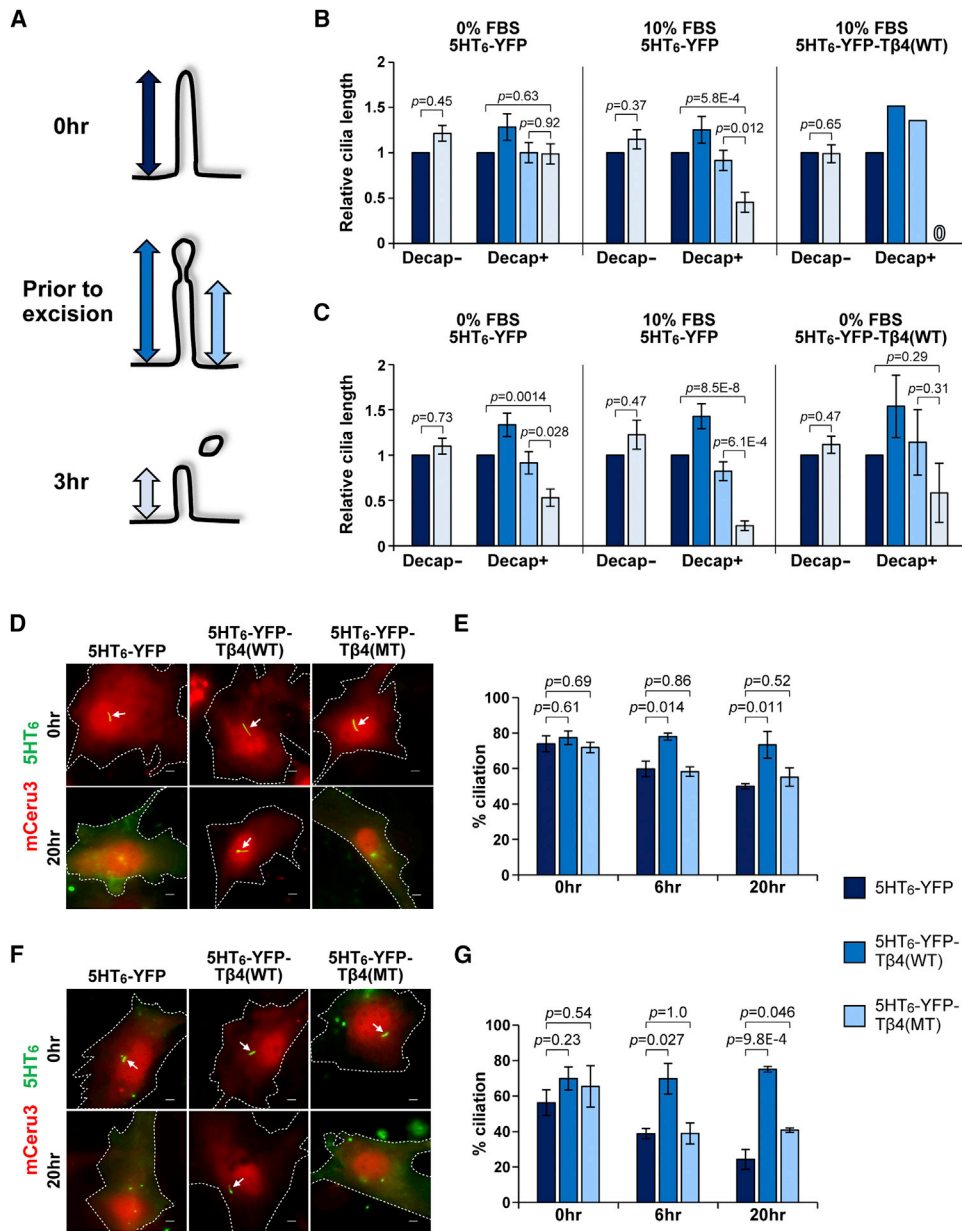
See also Figure S5 and Tables S1 and S2.

Figure 5. Inhibition of Cilia Decapitation Suppresses Growth-Stimulated Cilia Disassembly

(A) Schematic illustrating the time points when respective cilia lengths, indicated by double-headed arrows, were measured over a 3 hr live imaging period. Color coding for arrows applies to (B) and (C).

(B) Quantification of *Inpp5e*^{+/−} MEF cilia lengths over 3 hr imaging period. Cilia are classified according to occurrence of cilia decapitation, and cilia lengths are given as a ratio to cilia length at T = 0. Only a single cell was available for analysis under the category of "Decap+; 10% FBS 5HT$_6$-YFP-Tβ4(WT)" due to high efficacy of 5HT$_6$-YFP-Tβ4(WT) in inhibiting cilia decapitation. "0" indicates complete disassembly. Data in left and middle panels were derived from data in Figure 1D. (n = 26,11,19,22,9,1 cells; 1–5 experiments).

(C) Quantification of *Inpp5e*^{−/−} MEF cilia lengths over 3 hr imaging period, with similar data representation as in (B). Data in left and middle panels were derived from data in Figure 1D. (n = 8,16,8,20,11,3 cells; 2-5 experiments).

(D) Live fluorescence images of *Inpp5e*^{+/−} MEFs under indicated conditions at 0 and 20 hr of 10% FBS stimulation. Arrows mark cilia.

(E) Quantification of % cells possessing primary cilia, as in (D). (n = 167, 182, 162, 157, 153, 164, 176, 131, 139 cells from left to right; 3 experiments).

(F) Live fluorescence images of *Inpp5e*^{−/−} MEFs under indicated conditions at 0 and 20 hr of 10% FBS stimulation. Arrows mark cilia.

(G) Quantification of % cells possessing primary cilia, as in (F). (n = 165, 155, 112, 156, 107, 123, 146, 136, 144 cells from left to right; 3 experiments).

Data shown as mean ± SEM; Student's t tests were performed with p values indicated. In (B) and (C), Student's t tests were performed on absolute cilia lengths. Scale bars, 5μm.

cilia disassembly underscores how Inpp5e controls the disassembly process (Figures S2C and S2D).

Cilia Decapitation Ensures Timely Quiescence Exit

Since growth stimulation of quiescent cells would induce cell-cycle entry, we determined the timing of cilia decapitation in relation to cell cycle. Co-expression of Venus-p27K$^-$ (a G_0 marker) and mCherry-hCdt1(30/120) (a G_0/G_1 marker) enables cells in G_0, G_1, or S phase to be respectively labeled with Venus/mCherry, mCherry only, or null nuclear fluorescence (Oki et al., 2014). G_0-G_1 transit will be manifested as a steep decrease in Venus-p27K$^-$, while G_1-S transit will be marked by a subsequent abrupt decrease in mCherry-hCdt1(30/120). By considering the relative expression ratio of Venus-p27K$^-$ and mCherry-hCdt1(30/120), we arbitrarily defined Venus-p27K$^-$/mCherry-hCdt1(30/120) = 0.5 as the mid-point of G_0-G_1 transit.

We expressed these cell-cycle probes in Inpp5e$^{+/-}$ MEFs with either 5HT$_6$-mCeru3 or 5HT$_6$-mCeru3-Tβ4(WT) and subjected quiescent cells to a 10-hr growth stimulation. In 5HT$_6$-mCeru3-expressing cells, 20/25 (80%) cells underwent at least a single cilia decapitation event (Figures 6A, 6B, S6A, and S6B). Out of these 20 cells, 19 (95%) of them exhibited the first cilia decapitation event prior to G_0-G_1 transit, while one cell underwent cilia decapitation during the transit (Figures 6A, 6B, and S6A). Thus, growth stimulation at quiescence induces cilia decapitation in G_0 phase. We further compared the time taken by cells with intact or decapitated primary cilia to reach the G_0-G_1 transit midpoint upon growth stimulation. Within the cell population, which exhibited at least one cilia decapitation event at quiescence, 15/20 (75%) cells were determined to exit quiescence within 10 hr of growth stimulation (i.e., these cells demonstrated a sharp decrease in Venus-p27K$^-$ at some point), and they took an average time of 5.7 ± 0.4 hr to reach the G_0-G_1 transit mid-point (Figures 6A, 6B, 6E, and S6A and Movie S5). In contrast, 7/10 (70%) of 5HT$_6$-mCeru3-Tβ4(WT)-expressing cells suppressed for cilia decapitation were either not determined for quiescence exit (43% (3/7)) or took a prolonged time of 8.9 ± 0.4 hr to reach G_0-G_1 transit mid-point (57% (4/7)) (Figures 6C–6E and S6D and Movie S5). Thus, cilia decapitation is required by quiescent cells for timely G_1 entry.

Cilia Decapitation Modulates Gli Transcription Factor Activity

We speculated that cilia decapitation might promote quiescence exit through mitogenic Hedgehog (Hh) signaling (Roy and Ingham, 2002). We established an NIH/3T3 cell line stably expressing a GFP reporter driven by a minimal promoter and 8xGli-Binding-Site (GBS) sequence to measure Gli1/2 (but not Gli3) transcription activity in single cells (Sasaki et al., 1997; Stamataki et al., 2005). This reporter cell line was transfected with either 5HT$_6$-tagRFP, 5HT$_6$-tagRFP-Tβ4(WT), or 5HT$_6$-tagRFP-Tβ4(MT) prior to quiescence induction, and Gli1/2 activity in these cells was measured in response to growth stimulation (20% FBS) or Smoothened (Smo)-dependent Hh activation (SAG; Smo agonist). All three groups of cells similarly expressed a low basal level of GFP at quiescence (Figures 7A

and 7B). In SAG-positive controls, a modest increase in GFP fluorescence was detected at 8 hr post-stimulation across these cells, which robustly increased by 24 hr (Figures 7A and 7B). Remarkably, an 8-hr growth stimulation induced an intermediate GFP fluorescence increase in 5HT$_6$-tagRFP-expressing cells that was accompanied by an average decrease in cilia length (Figures 7A–7C). Similar observations were made for 5HT$_6$-tagRFP-Tβ4(MT)-expressing cells, whereas 5HT$_6$-tagRFP-Tβ4(WT)-expressing cells, which were suppressed for cilia decapitation, exhibited neither comparable changes in GFP fluorescence nor cilia length (Figures 7A–7C). Moreover, Smo inhibitor Vismodegib was able to abolish the GFP fluorescence increase in SAG-induced conditions, but not in FBS-treated conditions (Figures 7D and 7E). We also verified that an 8-hr treatment with 20% FBS did not promote Smo translocation into primary cilia (Figures 7F and 7G). Overall, these results implied a Smo-independent role of cilia decapitation in growth-induced Gli1/2 activation. To further verify this, we assessed how the expression of general Hh targets Gli1 and Ptch1 were affected by growth stimulation. Control treatment with SAG induced a robust increase in Gli1 and Ptch1 gene expression in NIH/3T3 at 8 hr. Interestingly, an ~2-fold increase in Ptch1 gene expression was observed in NIH/3T3 cells at 8-hr post-stimulation with 10% FBS, while no change was observed for Gli1 gene (Figure 7H). Growth-induced Ptch1 expression supports an increase in Gli1/2 activity. Lastly, a lack of Gli1 gene upregulation suggests that Gli1 activation upon growth stimulation would likely occur at the post-transcriptional level.

DISCUSSION

A primary cilium is traditionally defined by the presence of a microtubular axoneme and an absence of actin filaments. Here, we demonstrate that primary cilia possess capacity for actin polymerization under specific conditions. F-actin-powered cilia decapitation not only triggers resorption of the ciliary structure but also regulates proliferative signaling which connects the cilia life cycle and cell division cycle (Figure 7I).

The Molecular Players of Cilia Decapitation

Inpp5e and HDAC6 act in complementary pathways downstream of AurA to disassemble the ciliary structure. Earlier work determined that AurA phosphorylates Inpp5e to modulate its 5-phosphatase activity (Plotnikova et al., 2015), and we discovered that AurA also dictates Inpp5e distribution. It is therefore tempting to speculate that phosphorylated Inpp5e may have altered affinity against binding partners, which coordinate its ciliary localization (Humbert et al., 2012). Within the primary cilia, Inpp5e functions as a rheostat that tunes PI(4,5)P$_2$ required for actin polymerization. The resultant assembly of F-actin in distal cilia could be attributed to the presence of a bulky microtubular axoneme, which physically obstructs stable F-actin foci organization in the proximal ciliary lumen. Upon growth stimulation, concomitant HDAC6-dependent axonemal resorption and Inpp5e-dependent PI(4,5)P$_2$ redistribution could culminate in a position in distal cilia that is devoid of microtubules while harboring PI(4,5)P$_2$, permitting
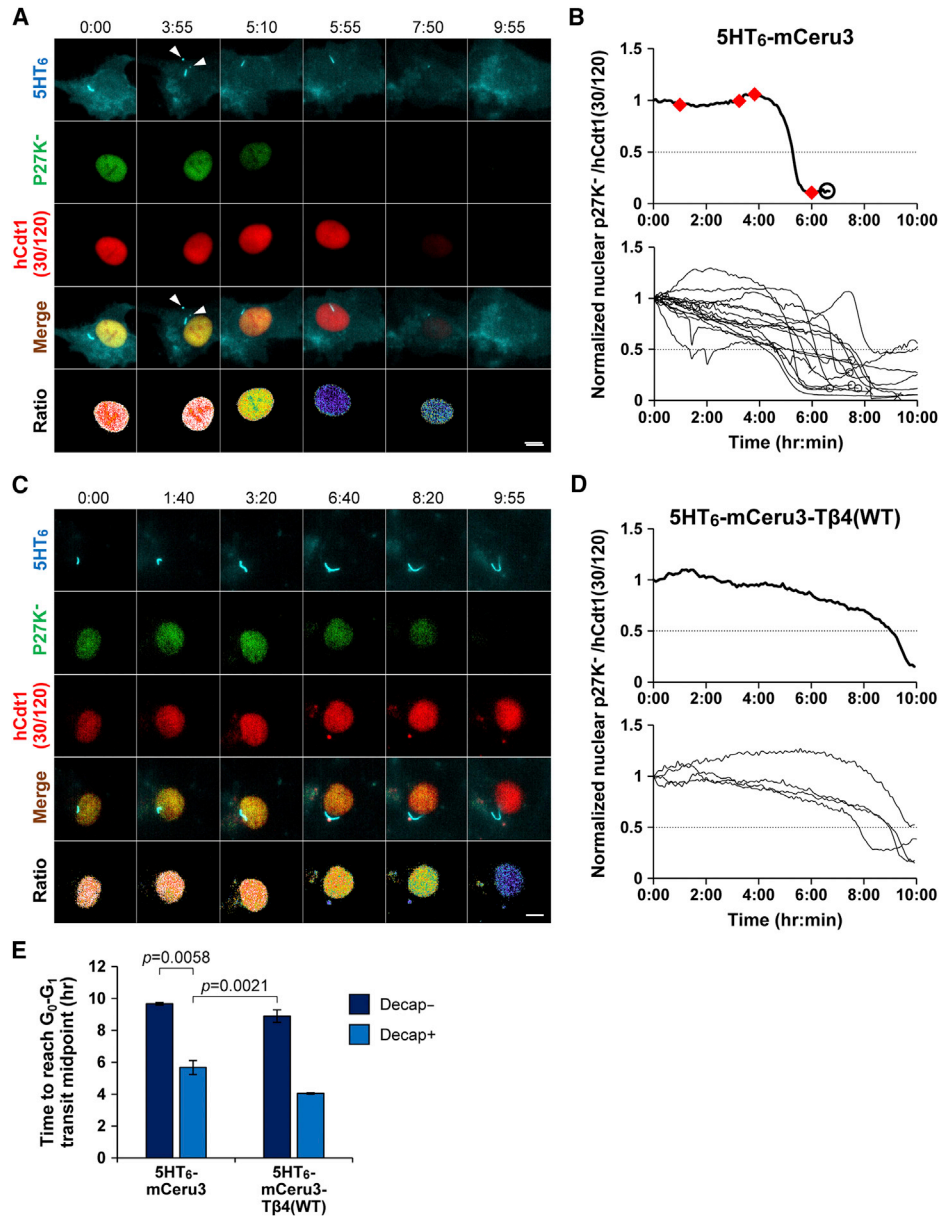
Figure 6. Cilia Decapitation Occurs in G_0 and Regulates G_1 Phase Entry

(A) Representative time-lapse images of prompt G_1 entry that occurs with cilia decapitation in *Inpp5e*$^{+/-}$ MEFs expressing 5HT$_6$-mCeru3. Venus-p27K$^-$ was abruptly degraded at ~5 hr post-FBS stimulation, and rapid mCherry-hCdt1(30/120) depletion ensued by ~8 hr post-FBS stimulation, indicating transit into G_1 and S phase, respectively. Images of each panel are scaled to same intensity range. Arrowheads indicate ciliary vesicles.

(B) Quantification of basal-normalized nuclear Venus-p27K$^-$/mCherry-hCdt1 ratio (pseudo-colored in [A]) over 10 hr. Top: plot for cell in (A). Red diamonds indicate cilia decapitation time points. Open circle marks beginning of mCherry-hCdt1(30/120) degradation. Bottom: plot for all 15 cells that were determined for quiescence exit within the 10 hr period (i.e., these cells demonstrated a sharp decrease in Venus-p27K$^-$ at some point). Cilia decapitation events not denoted here; refer to Figure S6A for individual plots. Open circle marks beginning of mCherry-hCdt1(30/120) degradation. Crosses mark end of imaging period.

(C) Representative time-lapse images of prolonged G_1 entry that occurs with suppressed cilia decapitation in *Inpp5e*$^{+/-}$ MEFs expressing 5HT$_6$-mceru3-Tβ4(WT). Note gradual Venus-p27K$^-$ degradation, which indicates delayed G_1 entry. Images of each panel are scaled to same intensity range.

(D) Quantification of basal-normalized nuclear Venus-p27K$^-$/mCherry-hCdt1 ratio (pseudo-colored in [C]) over 10 hr. Top: plot for cell in (C). No cilia decapitation was observed over the 10 hr imaging period. Bottom: plot for all four cells that were determined to exit quiescence; refer to Figure S6D for individual plots.

(E) Quantification of time duration to reach G_0-G_1 transit mid-point, derived from time points when basal-normalized p27K$^-$/hCdt1 = 0.5. Only cells that reached ratio value $\leq$ 0.5 by 10 hr were considered here. Data shown as mean ± SEM. Student's t tests were performed with p values indicated. (n = 2, 15, 4, 2 cells; 3-7 experiments).

Time in hr:min. Scale bars, 10 μm. See also Figure S6 and Movie S5.

A

GFP (A.U.): 500 ▸ 1200   700 ▸ 2500

B

C

D

GFP (A.U.): 400 ▸ 900

E

F

G

H

Ptch1   *Gli1*

I
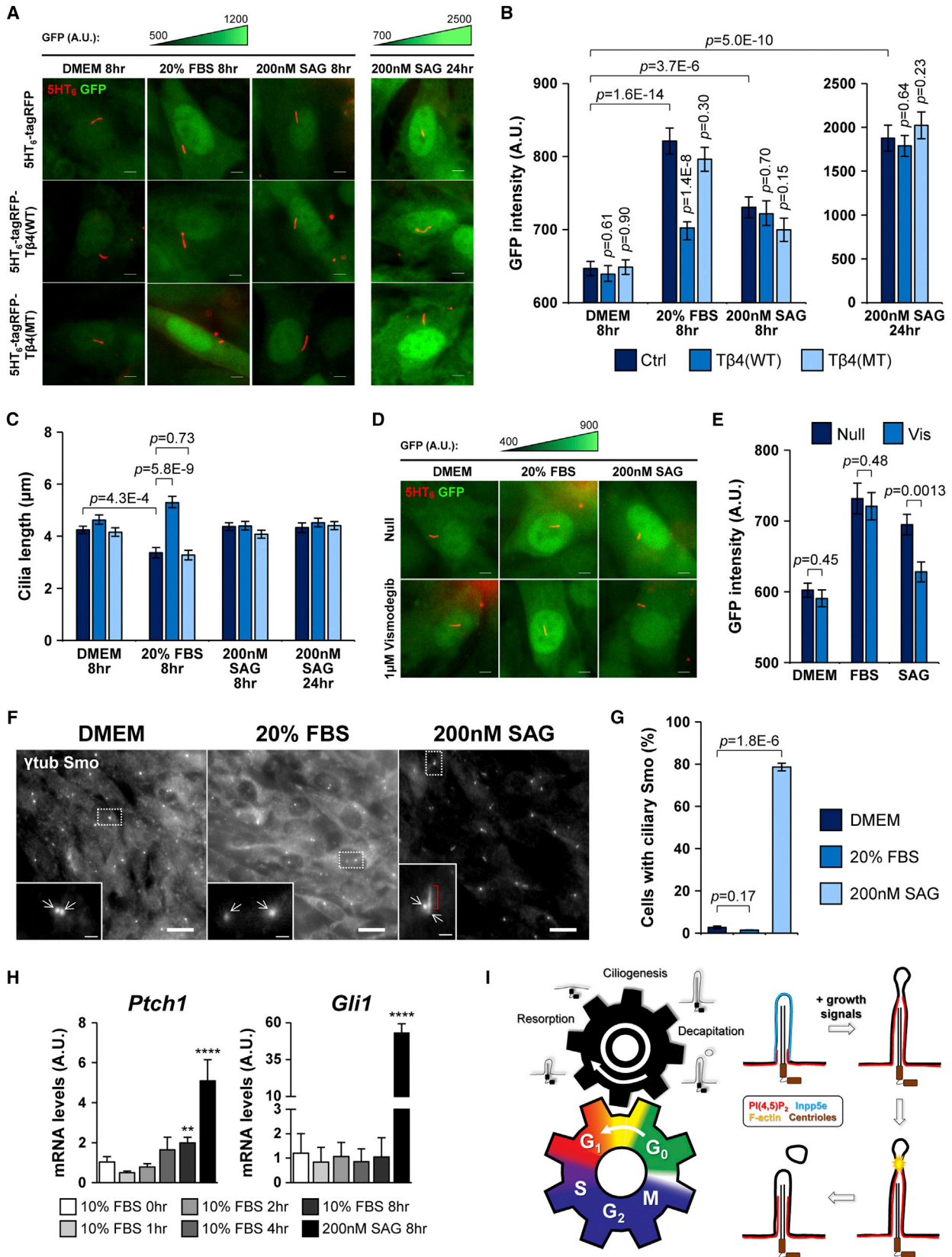
(legend on next page)

stable actin nucleation at that point. Moreover, the tip region of a primary cilium has been revealed as a sub-compartment harboring specific signaling molecules (He et al., 2014). The distal cilia may similarly possess properties promoting actin polymerization, and this is supported by our observed cofilin-1 enrichment in the tips of PI(4,5)P$_2$-elevated cilia (Figures S3B and S3D).

The Functional Role of IFT-B Elimination in Cilia Disassembly

Cilia decapitation could function as a ciliary outlet for IFT-B during cilia disassembly. Many components of IFT-B are associated with cilia growth; Ift81 and Ift74 constitute a tubulin-binding module that captures and delivers $\alpha\beta$-tubulin dimers to the plus end of ciliary axoneme for elongation (Bhogaraju et al., 2013). During the process of cilia resorption, the large pore size (7.9–9 nm) of a diffusion barrier positioned at the ciliary base would allow rapid diffusion of resorbed IFT-B constituents from the cytosol back into the ciliary lumen to result in inappropriate cilia re-growth (Breslow et al., 2013; Lin et al., 2013). Acute removal of IFT-B from primary cilia through decapitation could limit cilia re-growth, thereby playing an active, facilitating role in cilia disassembly. Upregulation of the ciliary IFT-B/IFT-A ratio by growth stimulation could enhance IFT-B removal from ciliary tips and could involve the serine/threonine protein kinase ICK, which is a candidate ciliary vesicle component involved in regulating the ciliary anterograde motor, Kif3a (Figure 4C and Table S2) (Chaya et al., 2014).

Cilia Decapitation as a Driver of Quiescence Exit

In differentiating neural progenitors, primary cilia dismantling as a result of apical abscission terminates mitogenic Hh signals for quiescence entry (Das and Storey, 2014). Conversely, we propose that cilia decapitation enhances Hh signaling to drive quiescence exit. Growth induction likely activates the mTOR signaling pathway in which S6K1 phosphorylates Gli1 to release it from Sufu inhibition (Wang et al., 2012), and active Gli1 could promote downstream cyclin D2 expression, which

functions in quiescence exit (Susaki et al., 2007; Yoon et al., 2002). Exploring cilia decapitation-mTOR signaling crosstalk thus holds exciting potential for understanding ciliary control of cell cycle and is motivated by (1) a role of primary cilia in mTOR signaling suppression via Lkb1 (Boehlke et al., 2010; Orhon et al., 2016) and (2) detection of an mTOR inhibitor, glycogen synthase kinase-3 beta (GSK3B), in ciliary vesicle proteomics (Figure 4C and Table S2) (Inoki et al., 2006). The Smo-independent role of growth stimulation on Gli1 activity is distinct from the Hh signaling repression caused by ciliary accumulation of Smo antagonists with complete Inpp5e loss (Chávez et al., 2015; Garcia-Gonzalo et al., 2015). Future work would entail understanding how Inpp5e loss affects Smo-independent Gli1 regulation and how growth-induced changes in ciliary PI(4,5)P$_2$ distribution could affect Smo antagonists in primary cilia.

Conclusion

Taken together, our present work describes a cell-autonomous role of cilia decapitation in cell-cycle regulation. Interestingly, earlier proposals characterized ciliary vesicles as signaling devices in algae and worms (Bergman et al., 1975; Cao et al., 2015; Wang et al., 2014, 2015; Wood and Rosenbaum, 2015; Wood et al., 2013). In line with these reports, mammalian primary cilia also associate with extracellular vesicles in vivo (Dubreuil et al., 2007; Hogan et al., 2009; Jacoby et al., 2009; Wood and Rosenbaum, 2015). Thus, the vesicles generated from cilia decapitation may engage in signal transmission in a non-cell-autonomous manner and exhibit potential as diagnostic readouts in development and cancer.

STAR★METHODS

Detailed methods are provided in the online version of this paper and include the following:

- KEY RESOURCES TABLE
- CONTACT FOR REAGENT AND RESOURCE SHARING

Figure 7. Growth-Induced Gli Activation Is Dependent on Cilia Decapitation

(A) Representative fluorescence images of NIH/3T3: 8xGBS-GFP reporter line under indicated conditions. GFP fluorescence intensities of the same column group are scaled to the same intensity ranges indicated above each group.

(B) GFP fluorescence intensity measurements, as in (A). (n = 70, 89, 72, 64, 73, 70, 61, 77, 61, 39, 56, and 59 cells from left to right; 4 experiments).

(C) Cilia length measurements in response to indicated stimuli and cilia-targeted probes; data derived from same experiments in (B).

(D) Representative fluorescence images of NIH/3T3: 8xGBS-GFP reporter line at 8 hr under indicated conditions. GFP fluorescence intensities are scaled to the same intensity range.

(E) GFP fluorescence intensity measurements, as in (D). (n = 39, 54, 48, 49, 43, and 44 cells from left to right; 3 experiments).

(F) γtub and Smoothened (Smo) immunofluorescence on NIH/3T3: 8xGBS-GFP reporter line upon 8 hr with indicated conditions. Insets are magnifications of dotted regions. Arrows indicate centrosomes. Red bracket indicates ciliary Smo signals.

(G) Scoring percentage of cells with ciliary Smo signals, as in (F). (n = 249, 206, 239 cells from left to right; 3 experiments).

(H) Quantitative real-time PCR assay for *Ptch1* and *Gli1* gene expression performed on NIH/3T3 post-stimulation with 10% FBS. An 8 hr 200 nM SAG positive control for Smo-dependent Hedgehog signaling activation was included. *Ubc* was used to normalize *Ptch1* and *Gli1* transcript levels. Data shown as mean ± SD; one-way ANOVA was performed to compare 0 hr 10% FBS samples with all other samples. **p < 0.01; ****p < 0.0001 (n = 8 experiments).

(I) Summary model of cilia decapitation during quiescence exit. (Left) Two meshing gears represent the mutual dependency between cell-division cycle and primary cilium life cycle. As known, growth induction (counterclockwise rotation of the bottom gear) promotes cilia disassembly (clockwise rotation of the top gear). The present study characterizes cilia decapitation as one of the key gear teeth enmeshing the two biological cycles. Cilia decapitation stimulates disassembly of cilia and also modulates cell proliferation by inducing G$_1$ entry. (Right) Growth-stimulated cilia decapitation occurs through four major steps: (1) Inpp5e depletion; (2) PI(4,5)P$_2$ elevation; (3) actin polymerization; (4) cilia tip excision.

In (B), (C), (E), (G), data are shown as mean ± SEM; Student's t tests were performed between indicated sample pairs (horizontal p values) or with respect to each 5HT$_6$-tagRFP condition (vertical p values). Scale bars indicate 5 μm in (A) and (D), 20 μm and 2 μm in (F) and (F) insets, respectively.

- EXPERIMENTAL MODEL AND SUBJECT DETAILS
  - Cell culture
- METHOD DETAILS
  - Transient and stable transfection
  - DNA plasmid construction
  - Generation of *Ift88*-KO mIMCD-3
  - Generation of Ift81:YNL knock-in mIMCD-3
  - Generation of NIH/3T3-Flp-In: 8xGBS-GFP and reporter assay
  - Immunofluorescence
  - Epi-fluorescence imaging
  - Confocal imaging
  - Structured illumination microscopy imaging
  - Quantitative image analyses
  - Ciliary vesicle collection
  - Western blotting
  - LC-MS/MS of proteins in pelleted conditioned culture media
  - Proteomic analyses
  - Quantitative real-time PCR
- QUANTIFICATION AND STATISTICAL ANALYSIS

SUPPLEMENTAL INFORMATION

Supplemental Information includes six figures, three tables, and five movies and can be found with this article online at http://dx.doi.org/10.1016/j.cell.2016.12.032.

REFERENCES

Basten, S.G., and Giles, R.H. (2013). Functional aspects of primary cilia in signaling, cell cycle and tumorigenesis. Cilia *2*, 6.

Bergman, K., Goodenough, U.W., Goodenough, D.A., Jawitz, J., and Martin, H. (1975). Gametic differentiation in Chlamydomonas reinhardtii. II. Flagellar membranes and the agglutination reaction. J. Cell Biol. *67*, 606–622.

Bhogaraju, S., Cajanek, L., Fort, C., Blisnick, T., Weber, K., Taschner, M., Mizuno, N., Lamla, S., Bastin, P., Nigg, E.A., and Lorentzen, E. (2013). Molecular basis of tubulin transport within the cilium by IFT74 and IFT81. Science *341*, 1009–1012.

Bielas, S.L., Silhavy, J.L., Brancati, F., Kisseleva, M.V., Al-Gazali, L., Sztriha, L., Bayoumi, R.A., Zaki, M.S., Abdel-Aleem, A., Rosti, R.O., et al. (2009). Mutations in INPP5E, encoding inositol polyphosphate-5-phosphatase E, link phosphatidyl inositol signaling to the ciliopathies. Nat. Genet. *41*, 1032–1036.

Boehlke, C., Kotsis, F., Patel, V., Braeg, S., Voelker, H., Bredt, S., Beyer, T., Janusch, H., Hamann, C., Gödel, M., et al. (2010). Primary cilia regulate mTORC1 activity and cell size through Lkb1. Nat. Cell Biol. *12*, 1115–1122.

Breslow, D.K., Koslover, E.F., Seydel, F., Spakowitz, A.J., and Nachury, M.V. (2013). An in vitro assay for entry into cilia reveals unique properties of the soluble diffusion barrier. J. Cell Biol. *203*, 129–147.

Cao, M., Ning, J., Hernandez-Lara, C.I., Belzile, O., Wang, Q., Dutcher, S.K., Liu, Y., and Snell, W.J. (2015). Uni-directional ciliary membrane protein trafficking by a cytoplasmic retrograde IFT motor and ciliary ectosome shedding. eLife *4*, e05242.

Chávez, M., Ena, S., Van Sande, J., de Kerchove d'Exaerde, A., Schurmans, S., and Schiffmann, S.N. (2015). Modulation of Ciliary Phosphoinositide Content Regulates Trafficking and Sonic Hedgehog Signaling Output. Dev. Cell *34*, 338–350.

Chaya, T., Omori, Y., Kuwahara, R., and Furukawa, T. (2014). ICK is essential for cell type-specific ciliogenesis and the regulation of ciliary transport. EMBO J. *33*, 1227–1242.

Christensen, S.T., Clement, C.A., Satir, P., and Pedersen, L.B. (2012). Primary cilia and coordination of receptor tyrosine kinase (RTK) signalling. J. Pathol. *226*, 172–184.

Das, R.M., and Storey, K.G. (2014). Apical abscission alters cell polarity and dismantles the primary cilium during neurogenesis. Science *343*, 200–204.

Dubreuil, V., Marzesco, A.M., Corbeil, D., Huttner, W.B., and Wilsch-Bräuninger, M. (2007). Midbody and primary cilium of neural progenitors release extracellular membrane particles enriched in the stem cell marker prominin-1. J. Cell Biol. *176*, 483–495.

Elias, J.E., and Gygi, S.P. (2007). Target-decoy search strategy for increased confidence in large-scale protein identifications by mass spectrometry. Nat. Methods *4*, 207–214.

Ezratty, E.J., Stokes, N., Chai, S., Shah, A.S., Williams, S.E., and Fuchs, E. (2011). A role for the primary cilium in Notch signaling and epidermal differentiation during skin development. Cell *145*, 1129–1141.

Francis, S.S., Sfakianos, J., Lo, B., and Mellman, I. (2011). A hierarchy of signals regulates entry of membrane proteins into the ciliary membrane domain in epithelial cells. J. Cell Biol. *193*, 219–233.

Garcia-Gonzalo, F.R., Phua, S.C., Roberson, E.C., Garcia, G., 3rd, Abedin, M., Schurmans, S., Inoue, T., and Reiter, J.F. (2015). Phosphoinositides Regulate Ciliary Protein Trafficking to Modulate Hedgehog Signaling. Dev. Cell *34*, 400–409.

Han, Y.-G., Kim, H.J., Dlugosz, A.A., Ellison, D.W., Gilbertson, R.J., and Alvarez-Buylla, A. (2009). Dual and opposing roles of primary cilia in medulloblastoma development. Nat. Med. *15*, 1062–1065.

He, M., Subramanian, R., Bangs, F., Omelchenko, T., Liem, K.F., Kapoor, T.M., and Anderson, K.V. (2014). The kinesin-4 protein Kif7 regulates mammalian Hedgehog signalling by organizing the cilium tip compartment. Nat. Cell Biol. *16*, 663–672.

Hogan, M.C., Manganelli, L., Woollard, J.R., Masyuk, A.I., Masyuk, T.V., Tammachote, R., Huang, B.Q., Leontovich, A.A., Beito, T.G., Madden, B.J., et al. (2009). Characterization of PKD protein-positive exosome-like vesicles. J. Am. Soc. Nephrol. *20*, 278–288.

Hui, C.C., and Angers, S. (2011). Gli proteins in development and disease. Annu. Rev. Cell Dev. Biol. *27*, 513–537.

Humbert, M.C., Weihbrecht, K., Searby, C.C., Li, Y., Pope, R.M., Sheffield, V.C., and Seo, S. (2012). ARL13B, PDE6D, and CEP164 form a functional network for INPP5E ciliary targeting. Proc. Natl. Acad. Sci. USA *109*, 19691–19696.

Humke, E.W., Dorn, K.V., Milenkovic, L., Scott, M.P., and Rohatgi, R. (2010). The output of Hedgehog signaling is controlled by the dynamic association between Suppressor of Fused and the Gli proteins. Genes Dev. *24*, 670–682.

Inoki, K., Ouyang, H., Zhu, T., Lindvall, C., Wang, Y., Zhang, X., Yang, Q., Bennett, C., Harada, Y., Stankunas, K., et al. (2006). TSC2 integrates Wnt and energy signals via a coordinated phosphorylation by AMPK and GSK3 to regulate cell growth. Cell *126*, 955–968.

Jacoby, M., Cox, J.J., Gayral, S., Hampshire, D.J., Ayub, M., Blockmans, M., Pernot, E., Kisseleva, M.V., Compère, P., Schiffmann, S.N., et al. (2009). INPP5E mutations cause primary cilium signaling defects, ciliary instability and ciliopathies in human and mouse. Nat. Genet. *41*, 1027–1031.

Käll, L., Canterbury, J.D., Weston, J., Noble, W.S., and MacCoss, M.J. (2007). Semi-supervised learning for peptide identification from shotgun proteomics datasets. Nat. Methods *4*, 923–925.

Kim, S., Zaghloul, N.A., Bubenshchikova, E., Oh, E.C., Rankin, S., Katsanis, N., Obara, T., and Tsiokas, L. (2011). Nde1-mediated inhibition of ciliogenesis affects cell cycle re-entry. Nat. Cell Biol. *13*, 351–360.

Lancaster, M.A., Schroth, J., and Gleeson, J.G. (2011). Subcellular spatial regulation of canonical Wnt signalling at the primary cilium. Nat. Cell Biol. *13*, 700–707.

Lin, Y.-C., Niewiadomski, P., Lin, B., Nakamura, H., Phua, S.C., Jiao, J., Levchenko, A., Inoue, T., Rohatgi, R., and Inoue, T. (2013). Chemically inducible diffusion trap at cilia reveals molecular sieve-like barrier. Nat. Chem. Biol. *9*, 437–443.

Mattila, P.K., and Lappalainen, P. (2008). Filopodia: molecular architecture and cellular functions. Nat. Rev. Mol. Cell Biol. *9*, 446–454.

Monje, M., Mitra, S.S., Freret, M.E., Raveh, T.B., Kim, J., Masek, M., Attema, J.L., Li, G., Haddix, T., Edwards, M.S.B., et al. (2011). Hedgehog-responsive candidate cell of origin for diffuse intrinsic pontine glioma. Proc. Natl. Acad. Sci. USA *108*, 4453–4458.

Nauli, S.M., Alenghat, F.J., Luo, Y., Williams, E., Vassilev, P., Li, X., Elia, A.E.H., Lu, W., Brown, E.M., Quinn, S.J., et al. (2003). Polycystins 1 and 2 mediate mechanosensation in the primary cilium of kidney cells. Nat. Genet. *33*, 129–137.

Oki, T., Nishimura, K., Kitaura, J., Togami, K., Maehara, A., Izawa, K., Sakaue-Sawano, A., Niida, A., Miyano, S., Aburatani, H., et al. (2014). A novel cell-cycle-indicator, mVenus-p27K-, identifies quiescent cells and visualizes G0-G1 transition. Sci. Rep. *4*, 4012.

Orhon, I., Dupont, N., Zaidan, M., Boitez, V., Burtin, M., Schmitt, A., Capiod, T., Viau, A., Beau, I., Kuehn, E.W., et al. (2016). Primary-cilium-dependent autophagy controls epithelial cell volume in response to fluid flow. Nat. Cell Biol. *18*, 657–667.

Pan, J., Wang, Q., and Snell, W.J. (2004). An aurora kinase is essential for flagellar disassembly in Chlamydomonas. Dev. Cell *6*, 445–451.

Paridaen, J.T.M.L., Wilsch-Bräuninger, M., and Huttner, W.B. (2013). Asymmetric inheritance of centrosome-associated primary cilium membrane directs ciliogenesis after cell division. Cell *155*, 333–344.

Phua, S.C., Lin, Y.C., and Inoue, T. (2015). An intelligent nano-antenna: Primary cilium harnesses TRP channels to decode polymodal stimuli. Cell Calcium *58*, 415–422.

Plotnikova, O.V., Golemis, E.A., and Pugacheva, E.N. (2008). Cell cycle-dependent ciliogenesis and cancer. Cancer Res. *68*, 2058–2061.

Plotnikova, O.V., Pugacheva, E.N., and Golemis, E.A. (2009). Primary cilia and the cell cycle. Methods Cell Biol. *94*, 137–160.

Plotnikova, O.V., Seo, S., Cottle, D.L., Conduit, S., Hakim, S., Dyson, J.M., Mitchell, C.A., and Smyth, I.M. (2015). INPP5E interacts with AURKA, linking phosphoinositide signaling to primary cilium stability. J. Cell Sci. *128*, 364–372.

Posor, Y., Eichhorn-Gruenig, M., Puchkov, D., Schöneberg, J., Ullrich, A., Lampe, A., Müller, R., Zarbakhsh, S., Gulluni, F., Hirsch, E., et al. (2013). Spatiotemporal control of endocytosis by phosphatidylinositol-3,4-bisphosphate. Nature *499*, 233–237.

Pugacheva, E.N., Jablonski, S.A., Hartman, T.R., Henske, E.P., and Golemis, E.A. (2007). HEF1-dependent Aurora A activation induces disassembly of the primary cilium. Cell *129*, 1351–1363.

Regl, G., Kasper, M., Schnidar, H., Eichberger, T., Neill, G.W., Ikram, M.S., Quinn, A.G., Philpott, M.P., Frischauf, A.-M., and Aberger, F. (2004). The zinc-finger transcription factor GLI2 antagonizes contact inhibition and differentiation of human epidermal cells. Oncogene *23*, 1263–1274.

Rohatgi, R., Milenkovic, L., and Scott, M.P. (2007). Patched1 regulates hedgehog signaling at the primary cilium. Science *317*, 372–376.

Roy, S., and Ingham, P.W. (2002). Hedgehogs tryst with the cell cycle. J. Cell Sci. *115*, 4393–4397.

Saarikangas, J., Zhao, H., and Lappalainen, P. (2010). Regulation of the actin cytoskeleton-plasma membrane interplay by phosphoinositides. Physiol. Rev. *90*, 259–289.

Sasaki, H., Hui, C., Nakafuku, M., and Kondoh, H. (1997). A binding site for Gli proteins is essential for HNF-3beta floor plate enhancer activity in transgenics and can respond to Shh in vitro. Development *124*, 1313–1322.

Singla, V., and Reiter, J.F. (2006). The primary cilium as the cell's antenna: signaling at a sensory organelle. Science *313*, 629–633.

Stamataki, D., Ulloa, F., Tsoni, S.V., Mynett, A., and Briscoe, J. (2005). A gradient of Gli activity mediates graded Sonic Hedgehog signaling in the neural tube. Genes Dev. *19*, 626–641.

Suh, B.C., Inoue, T., Meyer, T., and Hille, B. (2006). Rapid chemically induced changes of PtdIns(4,5)P2 gate KCNQ ion channels. Science *314*, 1454–1457.

Susaki, E., Nakayama, K., and Nakayama, K.I. (2007). Cyclin D2 translocates p27 out of the nucleus and promotes its degradation at the G0-G1 transition. Mol. Cell. Biol. *27*, 4626–4640.

Van Troys, M., Dewitte, D., Goethals, M., Carlier, M.F., Vandekerckhove, J., and Ampe, C. (1996). The actin binding site of thymosin beta 4 mapped by mutational analysis. EMBO J. *15*, 201–210.

Wang, Y., Ding, Q., Yen, C.J., Xia, W., Izzo, J.G., Lang, J.Y., Li, C.W., Hsu, J.L., Miller, S.A., Wang, X., et al. (2012). The crosstalk of mTOR/S6K1 and Hedgehog pathways. Cancer Cell *21*, 374–387.

Wang, W.-J., Tay, H.G., Soni, R., Perumal, G.S., Goll, M.G., Macaluso, F.P., Asara, J.M., Amack, J.D., and Tsou, M.-F.B. (2013). CEP162 is an axoneme-recognition protein promoting ciliary transition zone assembly at the cilia base. Nat. Cell Biol. *15*, 591–601.

Wang, J., Silva, M., Haas, L.A., Morsci, N.S., Nguyen, K.C.Q., Hall, D.H., and Barr, M.M. (2014). C. elegans ciliated sensory neurons release extracellular vesicles that function in animal communication. Curr. Biol. *24*, 519–525.

Wang, J., Kaletsky, R., Silva, M., Williams, A., Haas, L.A., Androwski, R.J., Landis, J.N., Patrick, C., Rashid, A., Santiago-Martinez, D., et al. (2015). Cell-Specific Transcriptional Profiling of Ciliated Sensory Neurons Reveals Regulators of Behavior and Extracellular Vesicle Biogenesis. Curr. Biol. *25*, 3232–3238.

Wong, S.Y., Seol, A.D., So, P.-L., Ermilov, A.N., Bichakjian, C.K., Epstein, E.H., Jr., Dlugosz, A.A., and Reiter, J.F. (2009). Primary cilia can both mediate and suppress Hedgehog pathway-dependent tumorigenesis. Nat. Med. *15*, 1055–1061.

Wood, C.R., and Rosenbaum, J.L. (2015). Ciliary ectosomes: transmissions from the cell's antenna. Trends Cell Biol. *25*, 276–285.

Wood, C.R., Huang, K., Diener, D.R., and Rosenbaum, J.L. (2013). The cilium secretes bioactive ectosomes. Curr. Biol. *23*, 906–911.

Yarar, D., Waterman-Storer, C.M., and Schmid, S.L. (2007). SNX9 couples actin assembly to phosphoinositide signals and is required for membrane remodeling during endocytosis. Dev. Cell *13*, 43–56.

Yeh, C., Li, A., Chuang, J.Z., Saito, M., Cáceres, A., and Sung, C.H. (2013). IGF-1 activates a cilium-localized noncanonical Gβγ signaling pathway that regulates cell-cycle progression. Dev. Cell *26*, 358–368.

Yoon, J.W., Kita, Y., Frank, D.J., Majewski, R.R., Konicek, B.A., Nobrega, M.A., Jacob, H., Walterhouse, D., and Iannaccone, P. (2002). Gene expression profiling leads to identification of GLI1-binding elements in target genes and a role for multiple downstream pathways in GLI1-induced cell transformation. J. Biol. Chem. *277*, 5548–5555.

Cell

STAR★METHODS

KEY RESOURCES TABLE

REAGENT or RESOURCE	SOURCE	IDENTIFIER
Antibodies		
Rabbit anti-Inpp5e	Jacoby et al., 2009	N/A
Rabbit anti-Smoothened	Rohatgi et al., 2007	N/A
Rabbit polyclonal anti-Arl13b	Proteintech	Cat#17711-1-AP; RRID: AB_2060867
Mouse monoclonal anti-acetylated tubulin clone 6-11B-1	Sigma	Cat#T7451; RRID: AB_609894
Mouse monoclonal anti-gamma tubulin clone GTU-88	Sigma	Cat#T6557; RRID: AB_477584
Mouse monoclonal anti-alpha tubulin clone DM1A	Sigma	Cat#T9026; RRID: AB_477593
Rabbit polyclonal anti-Ift81	Proteintech	Cat#11744-1-AP; RRID: AB_2121966
Rabbit polyclonal anti-Ift140	Proteintech	Cat#17460-1-AP: RRID: AB_2295648
Rabbit polyclonal anti-Ift88	ProteinTech	Cat#13967-1-AP; RRID: AB_2121979
Mouse monoclonal anti-Kif3A	BD Transduction	Cat#611508; RRID: AB_398968
Goat polyclonal anti-Gli3	R&D Systems	Cat#AF3690; RRID: AB_2232499
Rabbit polyclonal anti-Gli2	Abcam	Cat#ab26056; RRID: AB_2111901
Rabbit polyclonal Anti-Sufu	Humke et al., 2010	N/A
Rabbit polyclonal anti-actin	Sigma	Cat#A2066; RRID: AB_476693
Rabbit polyclonal anti-Ift122	ProteinTech	Cat#19304-1-AP
Mouse monoclonal anti-GAPDH clone 6C5	Millipore	Cat# MAB374; RRID: AB_2107445
Rabbit polyclonal anti-GFP	Medical & Biological Laboratories	Cat# 598; RRID: AB_591819
Chemicals, Peptides, and Recombinant Proteins		
Alisertib	MedChem Express	Cat#HY-10971
Tubacin	Cayman Chemical Company	Cat#13691
Vismodegib	LC labs	Cat#V-4050
SAG	Enzo Life Sciences	Cat#ALX-270-426
SAG	Cayman Chemicals	Cat#11914
Alexa Fluor 488 Phalloidin	ThermoFisher Scientific	Cat#A12379; RRID: AB_2315147
Experimental Models: Cell Lines		
$Inpp5e^{+/-}$ and $Inpp5e^{-/-}$ MEFs	This work	N/A
mIMCD-3	ATCC	CRL-2123; RRID: CVCL_0429
$Ift88$-KO mIMCD-3	This work	N/A
Ift81:YNL knock-in mIMCD-3	This work	N/A
hTERT RPE-1	ATCC	CRL-4000; RRID: CVCL_4388
NIH/3T3	ATCC	CRL-1658; RRID: CVCL_0594
NIH/3T3-Flp-in: 8xGBS-GFP	This work	N/A
Recombinant DNA		
PMXs-IP-mVenus-p27K⁻ plasmid	Oki et al., 2014	N/A
pCSII-EF-mCherry-hCdt1(30/120) plasmid	Brain Science Institute, Riken	GenBank: AB512478
5HT$_6$-YFP/mCeru3/tagRFP-Thymosinβ4(WT)	This work	N/A
5HT$_6$-YFP/mCeru3/tagRFP-Thymosinβ4(KK18,19EE; MT)	This work	N/A
5HT$_6$-YFP-Inpp5e(WT)	This work	N/A
5HT$_6$-YFP-Inpp5e(D477N; PD)	This work	N/A

(Continued on next page)

Continued

REAGENT or RESOURCE	SOURCE	IDENTIFIER
U6-gRNA(Ift88)/CMV-Cas9-2A-GFP	Sigma	Target ID: MM0000268220
U6-gRNA(Ift81)/CMV-Cas9-2A-GFP	This work	N/A
pCR-LA(Ift81)-YNL-RA(Ift81)	This work	N/A
Sequence-Based Reagents		
Primers used in this study	Table S3	N/A
gRNA targeting sequence: Ift88: GGAGGTCTTCTGCCATGAC	This work	N/A
gRNA targeting sequence: Ift81: ACAGGGCTCAGAGAACCAGC	This work	N/A
Software and Algorithms		
sgRNA designer	Broad Institute	http://portals.broadinstitute.org/gpp/public/analysis-tools/sgrna-design
Proteome Discoverer 1.4 software	ThermoFisher	https://www.thermofisher.com/
MASCOT	Matrix Science	http://www.matrixscience.com/
Percolator	Käll et al., 2007	http://percolator.ms/
MedCalc	MedCalc software	https://www.medcalc.org/
GraphPad Prism	GraphPad Software	https://www.graphpad.com/scientific-software/prism/

CONTACT FOR REAGENT AND RESOURCE SHARING

Further information and requests for reagents may be directed to, and will be fulfilled by the Lead Contact Takanari Inoue (jctinoue@jhmi.edu).

EXPERIMENTAL MODEL AND SUBJECT DETAILS

Cell culture

We derived MEFs from littermate E19.5 *Inpp5e*$^{+/-}$ and *Inpp5e*$^{-/-}$ embryonic tails using mouse protocols approved by the Institutional Animal Care and Use Committee (IACUC) at the University of California, San Francisco. Primary MEFs were maintained in DMEM, 15% FBS, and PenStrep, and immortalized by infection with a lentivirus expressing SV40 large T antigen.

Immortalized MEFs and NIH/3T3 were cultured in DMEM medium containing 10% FBS. mIMCD-3 and hTERT RPE-1 cells were cultured in DMEM/F-12 (1:1; Invitrogen) medium supplemented with 10% FBS. NIH/3T3-Flp-in: 8xGBS-GFP line was cultured in DMEM medium containing 10% FBS and 2mM GlutaMAX (GIBCO). In all experiments, cells were first induced for ciliogenesis by attaining quiescent state with following conditions: NIH/3T3 and MEFs were cultured in Opti-MEM I reduced serum medium (Thermofisher Scientific) with 0% FBS for 24 hr, NIH/3T3-Flp-in: 8xGBS-GFP line was cultured in DMEM containing 2mM GlutaMAX for 48 hr, and mIMCD-3 and hTERT-RPE1 were cultured in DMEM/F-12 (1:1; Invitrogen) medium containing 0%–0.1% FBS for 24 hr. To stimulate growth in quiescent cells, 10%–20% FBS were added to respective media depending on cell type. In some experiments, cells were treated with 200nM Alisertib (MedChem Express) and 2 μM Tubacin (Cayman Chemical Company). For live cell imaging, cells were plated on poly(d-lysine)-coated borosilicate glass Lab-Tek 8-well chambers (Thermo Scientific).

METHOD DETAILS

Transient and stable transfection

For transient transfection, cells were transfected with the respective DNA constructs by plating them directly in a transfection solution containing DNA plasmids and Xtremegene 9 (Roche). For mIMCD-3 and hTERT-RPE1 Arl13b-GFP stable lines, cells were transfected with Arl13b-pEGFP (Clontech) using FuGENE HD transfection reagents (Promega), and stable clones were selected in culture media containing 750 mg/ml G418.

DNA plasmid construction

To construct 5HT$_6$-YFP/mCeru3/tagRFP expression plasmids, we amplified stop codon-lacking mouse 5HT$_6$ cDNA with 5′ and 3′ AgeI cleavage sites by PCR and subcloned it into pEYFP/mCerulean3/tagRFP-C1 vectors (Clontech). To construct 5HT$_6$-YFP/mCeru3-PIPK and 5HT$_6$-YFP/mCeru3-PIPK(KD) expression plasmids, we digested DNAs encoding the wild-type or mutant forms of PIPK

from CFP-FKBP-PIPK (Suh et al., 2006) with 5′ EcoRI and 3′ BamHI cleavage sites and subcloned them into 5HT$_6$-YFP/mCeru3 expression plasmids. 5HT$_6$-mCherry was constructed by inserting stop codon-lacking mouse 5HT$_6$ cDNA into pmCherry-N1 using 5′ EcoRI and 3′ BamHI sites. To construct 5HT$_6$-YFP/mCeru3/tagRFP-Tβ4(WT), full-length thymosinβ4 cDNA was amplified from NIH/3T3 total cDNA using fwd: 5′-TTGGGAATTCGATGTCTGACAAACCCGAT-3′ and rev: 5′-CCAAGGATCCCGATTCGC CAGCTTGCTT-3′ primers, and inserted into 5HT$_6$-YFP/mCeru3/tagRFP using 5′ EcoRI and 3′ BamHI sites. Thymosinβ4 KK18,19EE mutant (Tβ4(MT)) was subsequently constructed via site-directed mutagenesis using fwd: 5′-TCGATAAGTCGAAGTTG GAGGAAACAGAAACGCAAGAG-3′ and rev: 5′-CTCTTGCGTTTCTGTTTCCTCCAACTTCGACTTATCGA-3′ primers. For 5HT$_6$-YFP-Inpp5e(WT), the human Inpp5e CaaX domain was first abolished using a C641A mutation to make Inpp5e non-membrane bound, and the resultant catalytic domain was amplified using fwd: 5′- TTGGGAATTCGCGGATCTTGCAGACTACAAGCTC-3′ and rev: 5′-AACCGGATCCTCAAGAAACGGAGGCGATGGTGC-3′ primers and inserted into 5HT$_6$-YFP using 5′ EcoRI and 3′ BamHI sites. Inpp5e D477N mutant was constructed via site-directed mutagenesis using fwd: 5′-AGGTGTTCTGGTTTGGAAACTTCA ACTTCCGCCTGAG-3′ and rev: 5′- CTCAGGCGGAAGTTGAAGTTTCCAAACCAGAACACCT-3′ primers. γ-tubulin-EGFP was constructed through cloning stop codon-lacking human TUBG2 cDNA into pEGFP-N2 plasmid using 5′ BglII and 3′ EcoRI sites. PMXs-IP-mVenus-p27K⁻ and pCSII-EF-mCherry-hCdt1(30/120) plasmids were kind gifts from Toshio Kitamura and Atsushi Miya-waki respectively.

Generation of *Ift88*-KO mIMCD-3
Ift88-KO mIMCD-3 was generated with a CRISPR/CAS9-based genome editing technique. mIMCD-3 cells were transfected transiently by an all-in-one plasmid U6-gRNA(Ift88)/CMV-Cas9-2A-GFP harboring CAS9, GFP, and guide RNA, available from Sigma-Aldrich. The target sequence of guide RNA was 5′-GGAGGTCTTCTGCCATGAC-3′. Cells expressing CAS9 was sorted next day with a fluorescence-activated cell sorter, ARIA (BD). The sorted cells were cloned in 96-well plate. Screening was performed with western blot analyses. Cells absent for Ift88 protein signals were further verified by analyzing target site DNA sequence in the genome.

Generation of Ift81:YNL knock-in mIMCD-3
Ift81:YNL knock-in mIMCD-3 cell line was generated using CRISPR/CAS9-based genome editing technique. mIMCD-3 cells were co-transfected with an all-in-one plasmid U6-gRNA(Ift81)/CMV-Cas9-2A-GFP harboring CAS9, GFP, and guide RNA, and a plasmid vector pCR-LA(Ift81)-YNL-RA(Ift81) harboring the left arm (834 bp), YNL (1614bp), and right arm (715 bp). The target sequence of gRNA was selected by using an algorism provided by Broad Institute (http://portals.broadinstitute.org/gpp/public/analysis-tools/sgrna-design). The target sequence of guide RNA was 5′-ACAGGGCTCAGAGAACCAGC-3′. Cells expressing CAS9 were sorted next day with a fluorescence-activated cell sorter, ARIA (BD). The sorted cells were cloned in 96-well plate. Initial screening was performed by PCR with primers: 5′-CAGTTGGCAGTTAAGAAACGGAG-3′; 5′-GTAGTCCACATGGAACAGAGGC-3′. Expression of Ift81-YNL was verified using western blot analyses with anti-GFP antibody (Medical & Biological Laboratories, Nagoya, Japan).

Generation of NIH/3T3-Flp-In: 8xGBS-GFP and reporter assay
A minimal promoter and 8xGLI-binding-site (GBS) sequences were inserted upstream of GFP within a pRRL.sin-18.PPT.GFP.pre lentiviral plasmid vector (Monje et al., 2011), and prepared lentiviruses were used to infect NIH/3T3-Flp-In cells (Life Technologies) in the presence of 4 μg/ml polybrene (Sigma). Cells were grown to confluence prior to serum starvation in the presence of 200nM SAG (Enzo Life Sciences) for 24 hr. GFP-expressing cells were single cell sorted into a 96-well plate using FACSAria II (BD Biosciences), and multiple single cell-derived clones were analyzed for SAG-induced GFP expression. For all reporter assay experiments, a specific clone with low basal GFP expression and high SAG-induced GFP expression was used. 40000 cells were seeded into one well of Lab-Tek 8-well chamber (Thermo Scientific), and cells were induced for quiescent state by culturing in serum starvation media (DMEM containing 2mM GlutaMAX) for 48 hr. Afterward, cells were treated with serum starvation media containing 20% FBS or 200nM SAG (Enzo Life Sciences), in the presence or absence of 1 μM Vismodegib (LC labs) for 8 hr or 24 hr. Cells were then fixed with 4% paraformaldehyde at room temperature for 10 min prior to imaging of reporter GFP expression.

Immunofluorescence
For most experiments, cells were fixed with 4% (v/v) paraformaldehyde at room temperature for 10 min, permeabilized with 0.1% (v/v) Triton X-100 for 5 min, blocked with 2% bovine serum albumin for 1 hr. Antibodies used are as follows: rabbit anti-Inpp5e (1:500; a kind gift from Stéphane Schurmans), rabbit anti-Smo (1:500; as reported in (Rohatgi et al., 2007)) rabbit anti-Arl13b (1:500; Proteintech 17711-1-AP), mouse anti-acetylated tubulin (1:1000; Sigma, T7451), mouse anti-gamma tubulin (1:1000; Sigma T6557). For immunofluorescence with rabbit anti-Ift81 (1:250; Proteintech,11744-1-AP), cells were fixed with 4% (v/v) paraformaldehyde for 10 min, prior to −20°C methanol fixation for 3 min. For immunofluorescence with rabbit anti-Ift140 (1:100; Proteintech, 17460-1-AP), cells were fixed with −20°C methanol for 3 min. F-actin probe, Alexa Fluor 488 Phalloidin (ThermoFisher Scientific) was also used.

Epi-fluorescence imaging
Live-cell imaging experiments were mostly performed using an IX-71 (Olympus) microscope with a 63x oil objective (Olympus) (with additional 1.6x optical zoom) and a Cool-SNAP HQ charge-coupled device camera (Photometrics) or an ORCA-Flash4.0 LT Digital CMOS camera (Hamamatsu). Time-lapse imaging experiments were performed with either 2 min or 5 min intervals, and between 3

and 11 0.5-μm z stacks were taken at each time point. Images shown were mostly maximum intensity projection. Micrographs were taken and analyzed using MetaMorph 7.5 imaging software (Molecular Devices).

Confocal imaging

Confocal live cell imaging of NIH/3T3 cilia decapitation was performed on FV1000 (Olympus, Japan) equipped with a stage top incubator (Tokai Hit, Japan). Confocal imaging of Arl13b+Actub- particles and live cell imaging of mIMCD-3 and hTERT RPE-1 cilia decapitation were performed using a LSM710 confocal microscope (Carl Zeiss microscopy) equipped with a Plan Aprochromat 63X oil immersion objective lens (NA 1.4) and processed using Zeiss Zen software. mIMCD-3 ciliary Ift81-YNL signals were visualized via direct 488-nm laser excitation of Venus on SP8 confocal microscope (Leica), and 3D image reconstruction were performed through volume rendering in 3D View software equipped in LAS X (Leica).

Structured illumination microscopy imaging

3D-SIM imaging was performed on an ELYRA S.1 microscope (Carl Zeiss microscopy) equipped with an Andor iXon 885 EMCCD camera, a 100X/1.40 NA oil-immersion objective and four laser beams (405, 488, 561, 642 nm). Serial z stack sectioning was carried out at 101 nm intervals. Z stacks were recorded with 3 phase-changes and 5 grating rotations for each section. The microscope was routinely calibrated with 100 nm fluorescent beads to calculate both lateral and axial limits of image resolution. Images were reconstituted with Zeiss Zen software. 3D rendering was produced by using Imaris 7.4.2 (Bitplane). Images were extracted from Imaris and then used to obtain the final images and movies used in the figures.

Quantitative image analyses

Inpp5e, Ift81 and Ift140 ciliary signals were quantified via subtraction of ciliary fluorescence signals from vicinity background signals; the boundary of ciliary axoneme was defined by Actub immunofluorescence, while γtub immunofluorescence enables distinguishing between ciliary base and tip. For ciliary Ift81-YNL measurements, each cilium was divided into 10 equal compartments along cilia length. YNL fluorescence intensities along cilia length was obtained using a line scan spanning from base to tip of each primary cilium, and mean YNL fluorescence intensity in each compartment was obtained by averaging across entire sample. Total YNL fluorescence intensity in cilium was calculated by integrating fluorescence intensities across all 10 compartments. Mean YNL fluorescence intensity distribution along cilia length was obtained by expressing mean YNL fluorescence intensity in each compartment as a percentage of Total YNL fluorescence intensity in cilium.

For relative ciliary PH(PLCδ) and small GTPase accumulation measurements, cilia length was measured by tracing a line along the ciliary marker signal, and PH(PLCδ)/small GTPase signal length was measured analogously and expressed as a ratio to cilia length.

Probes were scored as cilia-localized if probe fluorescence signals were co-localized with 5HT$_6$ or Arl13b fluorescence signals in x-, y- and z- planes. Cell-associated ciliary vesicles were either defined as Arl13b+Actub- particles (on fixed cells) or 5HT$_6$/Arl13b-YFP-positive particles that were associated with cell surface. To determine mid-point of G_0-G_1 transit, 10 hr time series of nuclear Venus-p27K$^-$ and mCherry-hCdt1(30/120) fluorescence signals were subtracted with background signals, divided to obtain Venus-p27K$^-$/mCherry-hCdt1(30/120) signal ratio values, and further normalized with basal ratio values at T = 0. For 8xGBS-GFP Gli activity reporter measurements, average nuclear GFP signal in best-focused z-plane was measured for each cell under specified conditions, since: (1) expressed GFP show nuclear enrichment in NIH/3T3 cells (2) high cell densities preclude ability to measure whole-cell signals.

It is of note that we occasionally observed primary cilia of fibroblasts extending from the ventral cell surface and adhering to underlying substratum. Subsequent cellular movements could result in mechanical pulling and breaking of primary cilia (Figure S1K). Care was taken to exclude instances of passive cilia breaking throughout all experiments.

Ciliary vesicle collection

FBS used for vesicle collection was pre-depleted via overnight centrifugation at 100,000 xg to remove FBS-intrinsic tiny vesicles, exosomes and ectosomes. Wild-type or *Ift88*-KO mIMCD-3 cells were subjected to serum starvation by reducing FBS concentration to 0%–0.1% for 12-24 hr after reaching confluence. Culture media were then replaced by fresh media containing 0%–0.1% or 10% pre-depleted FBS. Conditioned culture media were collected 24 to 30 hr later. Small vesicles released from cultured cells into media were collected through a three-step centrifugation. Culture media were first centrifuged at 2,000 xg for 20 min to remove large cell debris. The supernatant of the first centrifuge was further centrifuged at 10,000 xg for 30 min. The supernatant of the second centrifuge was centrifuged at 100,000 xg for 3 hr with MLA-55 angle rotor (Beckman). Pellets were rinsed once with PBS, and then subjected to western blotting or proteomics.

Western blotting

Collected small vesicles were resolved in 1.5x SDS sample buffer. Cultured cells were also lysed with the same buffer. Extracted proteins were denatured at 95°C for 5 min. Proteins were separated with SDS-PAGE, and transferred to PVDF membrane (Millipore). The membrane was blocked with 10% goat serum or 5% bovine serum albumin. The blocked membrane was incubated with primary antibodies in the blocking solution at 4°C overnight. Primary antibodies used were as follows: rabbit anti-Ift88 (1:2000; ProteinTech, 13967-1-AP); mouse anti-Kif3A (1:2000; BD Transduction, 611508); goat anti-Gli3 (1:200; R&D Systems, AF3690); rabbit anti-Gli2 (1:1000; Abcam, ab26056); rabbit anti-Sufu (1:2500; as reported in (Humke et al., 2010)); rabbit anti-Arl13b (1:1000; ProteinTech,

17711-1-AP); rabbit anti-actin (1:2000; Sigma, A2066); rabbit anti-Ift122 (1:2000; ProteinTech, 19304-1-AP); rabbit anti-Ift140 (1:2000; ProteinTech, 17460-1-AP); mouse anti-α-tubulin (1:10000; Sigma, T9026); mouse anti-GAPDH (1:2000; Millipore, MAB374). The primary antibodies were labeled with horseradish peroxidase-conjugated secondary antibodies (Jackson Immuno Lab). Signals were developed with enhanced chemiluminescent substrate (GE) and detected with a cooled CCD camera system, LAS-3000 mini (Fuji film). Band intensities were quantified with free software, ImageJ.

LC-MS/MS of proteins in pelleted conditioned culture media

Collected vesicles were lysed in 50 mM Tris, pH 8.0, containing 1.5% Triton X-100 with vigorous vortexing. Detergent and salt were removed with 2-D Clean-Up kit (GE Healthcare), and with cold acetone if further removal of detergent was required. Protein pellets were resolved in 50 mM NH_4HCO_3 with vigorous vortexing. The proteins were subjected to reductive alkylation of sulfur group with iodoacetamide (ThermoFisher), and then digested with trypsin (ThermoFisher) at 37°C overnight. Digested peptides were desalted by means of C-18 column (ThermoFisher) with 5% acetonitrile/0.5% trifluoroacetic acid used as wash buffer, and eluted with 70% acetonitrile. The acetonitrile was evaporated with a Speed-Vac concentrator (Tomy), and the eluted peptides were resolved in 0.1% formic acid.

The peptides were analyzed with a Q Exactive-Orbitrap mass spectrometer (ThermoFisher) connected to EASY-nLC liquid chromatography (ThermoFisher). Peptides were loaded into a micro capillary column (NTCC-360; Nikkyo Technos, Japan) of 75 μm inner diameter, and separated with a linear gradient of acetonitrile from 0 to 35% in 0.1% formic acid at a flow rate of 325 nL/min. Separated peptides were ionized with Nanospray Flex Ion Source, NSI (ThermoFisher) at spray voltage of 2.0 kV. Full mass spectra were acquired with a resolution of 70,000, a maximum injection time of 60 msec, and a scan range between m/z 350 to 1800, at positive ion mode. dd-MS^2 was acquired with a resolution of 17,500, a maximum injection time of 60 msec,and an isolation window of 2.0 m/z. All processes were operated with software Xcalibur^{TM} (ThermoFisher).

Proteomic analyses

Data acquired with LC-MS/MS were analyzed with Proteome Discoverer 1.4 software (ThermoFisher). All parameters for Spectrum Selector were set to default values. Identification of peptide/protein was carried out by means of MASCOT (MatrixScience) with Swiss-Prot used as database. Mass tolerances were 10 ppm for precursor mass and 0.02 Da for fragment mass. A miscleavage was allowed. Obtained peptide lists were validated by Percolator (Käll et al., 2007) based on q-values with a stringent threshold of target false discovery rate (FDR) of 1% using reverse decoy database (Elias and Gygi, 2007). The label-free semi-quantification was performed by using the precursor ions area detector (PIAD) node mounted in Proteome Discoverer 1.4.

Proteins that were detected at least two times in 9 independent experiments for serum-stimulated wild-type or *Ift88*-KO mIMCD-3 cells or 6 independent experiments for serum-starved wild-type mIMCD-3 cells were selected. The protein list and area values were exported as a table for further analyses in Microsoft Excel. Zero area values were replaced with one tenth of minimal area value of each sample for calculating fold changes. Ratio of mean area values were calculated for serum-stimulated wild-type versus *Ift88*-KO cells (WT/Ift88-KO) and for serum-stimulated versus serum-starved wild-type cells (10%/0.1%). Ratios were converted to logarithm to the base 2 (log$_2$), and Z-scores were calculated.

Quantitative real-time PCR

NIH/3T3 cells were seeded in OptiMEM (Thermo Fisher Scientific) for 24 hr to induce ciliogenesis at quiescent state. Cells were subsequently treated with DMEM containing 10% FBS for 0, 1, 2, 4, and 8 hr prior to sample collection. As a positive control, cells were also treated with 200 nM SAG (Cayman Chemicals) for 8hr. Cells were lysed with Buffer RLT, and RNA samples were isolated with the RNeasy Mini Kit with DNase I digestion (QIAGEN). Samples were reverse transcribed using the iScript cDNA synthesis kit (BioRad). Gli1 (F: 5′-GGATGAAGAAGCAGTTGGGA-3′; R: 5′-ATTGGATTGAACATGGCGTC-3′) and Ptch1 (F: 5′-CTCTGGAGCAGATTTC CAAGG-3′; R: 5′-TGCCGCAGTTCTTTTGAATG-3′) primers were used to test for Hedgehog signaling activation. Ubc primers (F: 5′-TCCAGAAAGAGTCCACCCTG-3′; R: 5′-GACGTCCAAGGTGATGGTCT-3′) were used to normalize *Gli1* and *Ptch1* transcript levels. Transcripts were quantified using SYBR-GreenER (Thermo Fisher Scientific) on a 7900HT Fast Real-Time PCR system (Thermo Fisher Scientific).

QUANTIFICATION AND STATISTICAL ANALYSIS

Statistical parameters including the definition and exact values of n (number of cells and experiments), distribution and deviation are reported in figures and corresponding legends. Most data are represented as mean ± SEM using two-tailed Student's t tests. Probability data in Figures 3 and S3 were analyzed using statistical risk ratio analyses; probability was determined by dividing number of positives by total number of cells analyzed, and relative risk was determined by dividing probability value in each test condition by that of control condition. Mass spectrometry signal area ratios were presented with Z-scores in Table S2. Z-scores in Figure 4D and data in Figure S5N were analyzed using Mann-Whitney U-test. Quantitative real-time PCR assays in Figure 7H were analyzed using one-way ANOVA. Statistical analyses were performed in Microsoft Excel, MedCalc or GraphPad Prism.
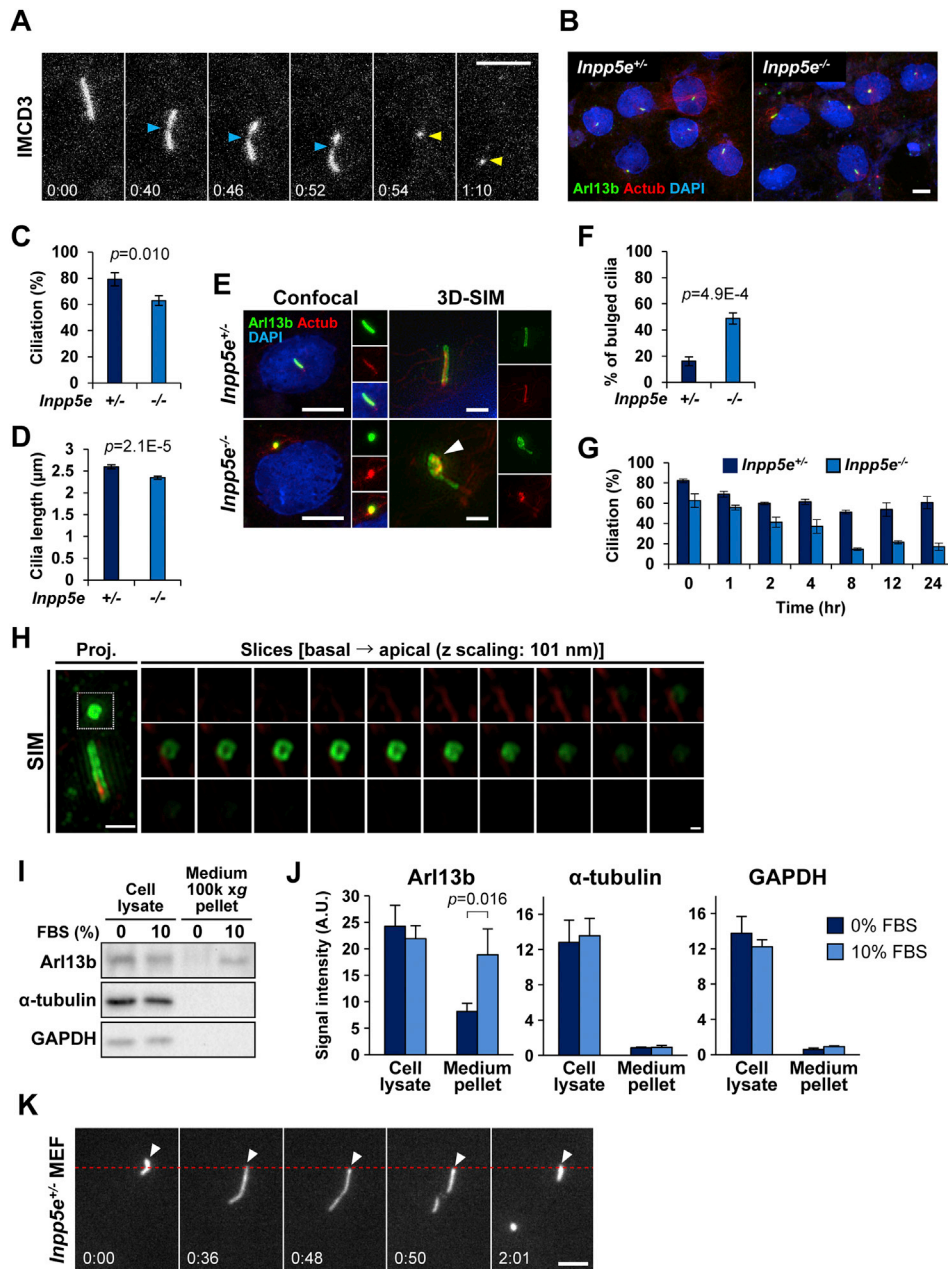
Figure S1. Characterization of Cilia Decapitation and *Inpp5e^+/−* and *Inpp5e^−/−* MEFs, Related to Figure 1

(A) Time-lapse images of a mIMCD-3 primary cilium expressing Arl13b-GFP at quiescent state (0% FBS). Blue arrows indicate membrane thinning prior to excision. Yellow arrowheads indicate excised cilium tip.

(B) Representative confocal images of Arl13b and Actub immunofluorescence in *Inpp5e^+/−* MEFs and *Inpp5e^−/−* MEFs at quiescent state. Nuclei labeled with DAPI.

(C) Quantification of % ciliation in quiescent *Inpp5e^+/−* and *Inpp5e^−/−* MEFs. A primary cilium is defined by positive labeling with Arl13b and Actub immuno-fluorescence. Data are represented as mean ± SEM. A two-tailed Student's t test was performed with p values indicated. (n = 323, 374 cells; 3 experiments).

(D) Quantification of Arl13b-labeled cilia lengths in quiescent *Inpp5e^+/−* and *Inpp5e^−/−* MEFs. Data are represented as mean ± SEM. A two-tailed Student's t test was performed with p values indicated. (n = 271, 353 cells; 3 experiments).

(E) Confocal and SR-SIM images of Arl13b and Actub immunofluorescence in *Inpp5e^+/−* MEFs and *Inpp5e^−/−* MEFs. Insets are magnified images of respective cilia. White arrowhead indicates bulged ciliary tip in *Inpp5e^−/−* MEFs.

(F) Quantification of % cells displaying bulged ciliary tips as in (E). Data are represented as mean ± SEM. A two-tailed Student's t test was performed with p values indicated. (n = 323, 374 cells; 3 experiments as in (B)).

(G) Quantification of % ciliation in *Inpp5e^+/−* and *Inpp5e^−/−* MEFs at indicated time points post-stimulation with 10% FBS. Data are represented as mean ± SEM (n = 271, 353 cells; 3 experiments).

(H) Z series of SR-SIM images of an Arl13b+ and Actub- particle.

(I) Representative western blots of Arl13b, α-tubulin and GAPDH proteins in collected cell lysates and pelleted conditioned culture media from mIMCD-3 cells treated with 0% (instead of 0.1%) or 10% FBS for 12 hr. Related to Figure 1H.

(J) Quantification of respective band signal intensities in (I). Data are shown as mean ± SEM. A two-tailed Student's t test was performed with *p* values indicated. (n = 4 experiments).

(K) Representative time-lapse images of a ventral-positioned *Inpp5e*$^{+/-}$ MEF primary cilium passively breaking as a result of non-specific adhesion and immobilization to underlying substratum. Cell was expressed with 5HT$_6$-YFP. Arrowheads indicate cilia tip. Red dotted line marks position of immobilization. See also Methods under "Quantitative image analyses."

Time in hr:min in (A) and (K). Scale bars indicate 5 um in (A) and (K), 10um in (E) left panel, 1um in (E) right panel, 1 μm in (H) left panel and 0.2 μm in (H) right panel.
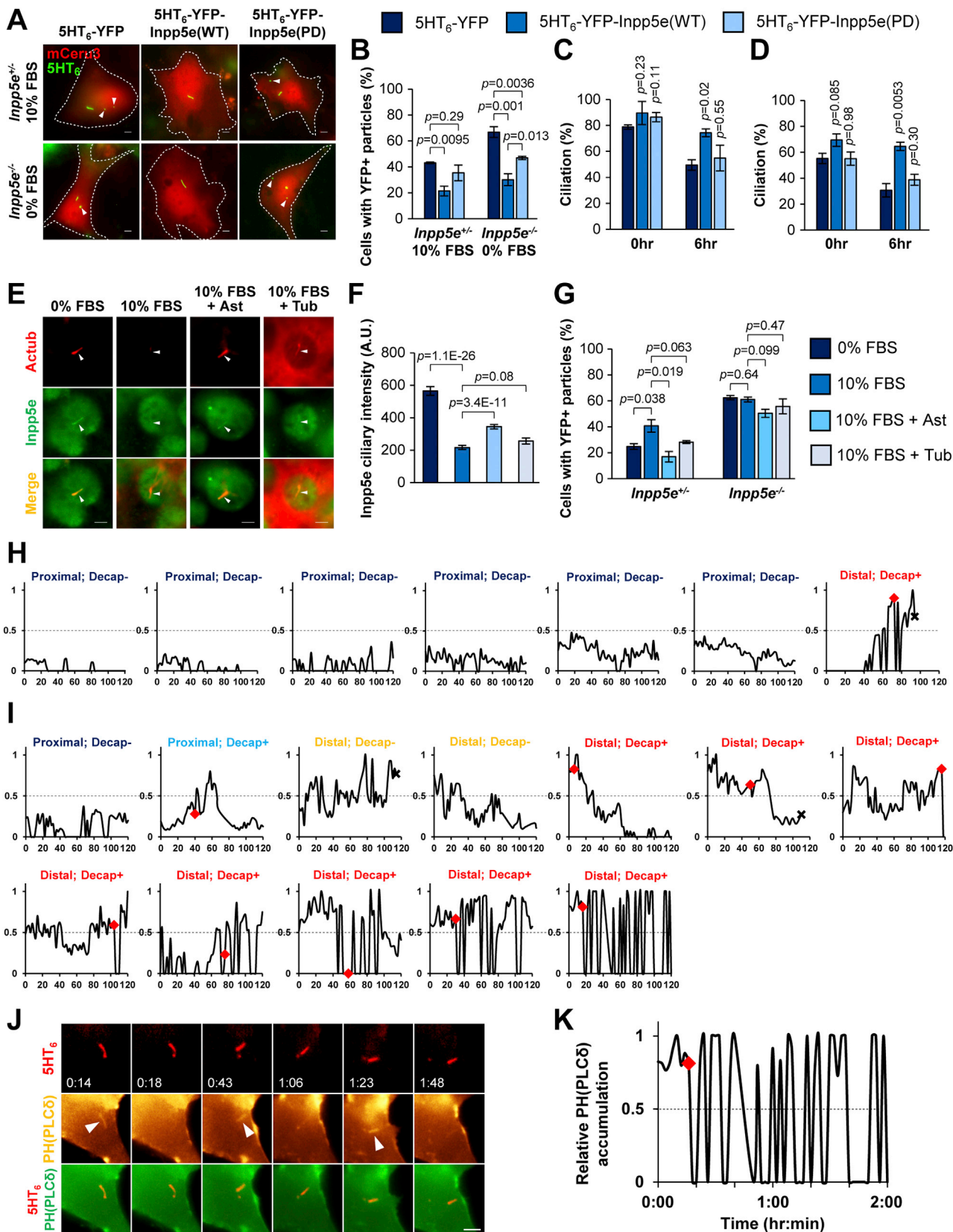
Figure S2. AurA-Dependent Ciliary Inpp5e Depletion Re-organizes Ciliary PI(4,5)P$_2$, Related to Figure 2

(A) Live fluorescence images of *Inpp5e*$^{+/-}$ MEFs or *Inpp5e*$^{-/-}$ MEFs expressing 5HT$_6$-YFP, 5HT$_6$-YFP-Inpp5e(WT) or 5HT$_6$-YFP-Inpp5e(PD) with cytosolic mCeru3 respectively after 4 hr of 10% FBS stimulation or at quiescent state (0% FBS). White dashed lines delineate cells. White arrowheads indicate cell-associated YFP+ particles that were likely vesicles released from primary cilia.

(B) Quantification of % cells with associated extracellular YFP+ particles under indicated conditions, as in (A). Color coding as in panel above. Data are represented as mean ± SEM. Two-tailed Student's t tests were performed with *p* values indicated. (n = 111, 73, 92, 94, 88, 74 cells for respective data from left to right; 4 experiments).

(C) Quantification of % ciliation in *Inpp5e*$^{+/-}$ MEFs expressing 5HT$_6$-YFP, 5HT$_6$-YFP-Inpp5e(WT) or 5HT$_6$-YFP-Inpp5e(PD) with cytosolic mCeru3 at 0 hr and 6 hr of 10% FBS stimulation. Color coding as in panel above. Data are represented as mean ± SEM. Two-tailed Student's t tests were performed with respect to each 5HT$_6$-YFP condition, *p* values indicated. (n = 88, 54, 49, 66, 35, 44 cells for respective data from left to right; 2 experiments).

(D) Quantification of % ciliation in *Inpp5e*$^{-/-}$ MEFs expressing 5HT$_6$-YFP, 5HT$_6$-YFP-Inpp5e(WT) or 5HT$_6$-YFP-Inpp5e(CD) with cytosolic mCeru3 at 0 hr and 6 hr of 10% FBS stimulation. Color coding as in panel above. Data are represented as mean ± SEM. Two-tailed Student's t tests were performed with respect to each 5HT$_6$-YFP condition, *p* values indicated. (n = 94, 49, 57, 100, 55, 70 cells for respective data from left to right; 3 experiments).

(E) Actub and Inpp5e immunofluorescence of *Inpp5e*$^{+/-}$ MEFs treated with 0% FBS, 10% FBS, 10% FBS +200nM Alisertib (Ast), or 10% FBS + 2 μM Tubacin (Tub) for 4 hr. Images within Actub and Inpp5e image panels are scaled to same intensity range, while Actub signals are adjusted in Merge to visualize axoneme. Arrowheads indicate cilia.

(F) Signal intensity measurements of Inpp5e immunofluorescence in primary cilia (cilia - vicinity background) under indicated conditions, as in (E). Color coding as in panel on the right. Data are represented as mean ± SEM. A two-tailed Student's t test was performed with *p* values indicated. (n = 190, 169, 173, 106 cells for respective data from left to right; 3 experiments).

(G) Quantification of % cells with associated extracellular YFP+ particles in *Inpp5e*$^{+/-}$ MEFs and *Inpp5e*$^{-/-}$ MEFs expressing 5HT$_6$-YFP with cytosolic mCeru3 after 4 hr in 0% FBS, 10% FBS, 10% FBS + 200nM Ast, or 10% FBS + 2 μM Tub. Color coding as in panel on the right. Data are represented as mean ± SEM. A two-tailed Student's t test was performed with *p* values indicated. (n = 124, 131, 112, 121, 48, 54, 47, 37 cells for respective data from left to right; 2-3 experiments).

(H and I) Time-lapse measurements of ciliary PH(PLCδ) accumulation in *Inpp5e*$^{+/-}$ MEFs at (H) quiescent state (as shown in Figure 2D) or (I) growth-stimulated state (as shown in Figure 2F). Horizontal axes indicate time(min); vertical axes indicate ciliary PH(PLCδ) accumulation expressed as a ratio of cilium length. Color coding as used in Figure 2G. Dotted line divide proximal half (0-0.5) and distal half (0.5-1.0) of cilium. "X"s indicate end of imaging period. Data for (I) were between 0 hr and 2 hrs, 2hrs and 4hrs, or 4hrs and 6hrs post-stimulation with 10% FBS.

(J) An example of growth-stimulated primary cilia exhibiting PI(4,5)P$_2$ oscillation post-decapitation. White arrowheads indicate ciliary PH(PLCδ).

(K) Time-lapse measurements of PH(PLCδ) accumulation in cilium in (C), expressed as relative ratio of cilium length. Red diamond marks time point of decapitation.
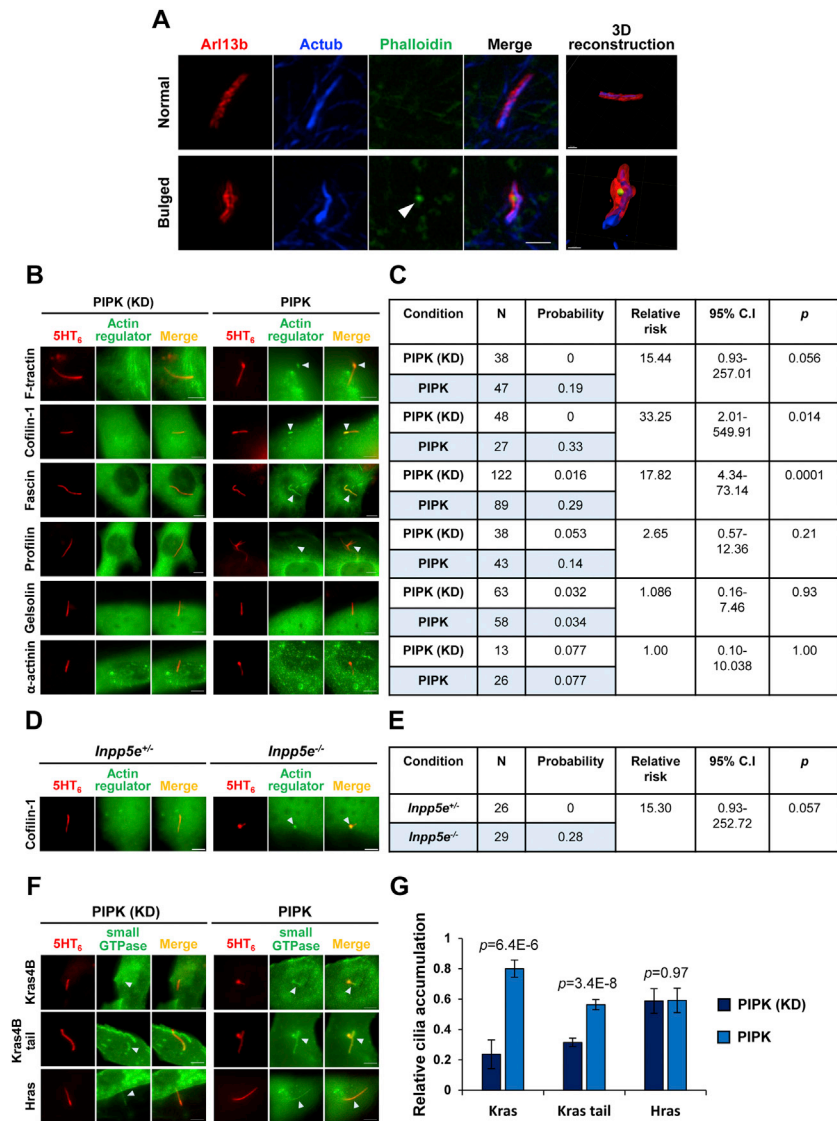
Time in hr:min. Scale bars indicate 5 μm.

Figure S3. PI(4,5)P$_2$ Regulates Ciliary Localization of F-Actin, Actin Regulatory Proteins, and Small GTPases, Related to Figure 3

(A) SR-SIM images of Arl13b, Actub and phalloidin immunofluorescence in normal and bulged cilia of $Inpp5e^{-/-}$ MEFs. Rightmost panel are IMARIS 3D reconstructions of "Merge" images. Arrowhead indicates ciliary phalloidin signals.

(B) Live fluorescence images of NIH/3T3 expressing 5HT$_6$-mCeru3-PIPK or 5HT$_6$-mCeru3-PIPK(KD) and respective YFP-tagged actin sensor (F-tractin) or actin regulators. White arrowheads indicate ciliary localization of respective proteins. Cofilin-1 was generally observed to accumulate at ciliary tip, while fascin was detected along ciliary length.

(C) Relative risk ratio analyses on the effect of differential ciliary PI(4,5)P$_2$ in influencing intraciliary F-actin or actin regulator incidence, for corresponding horizontal image rows in (B).

(D) Live fluorescence images of $Inpp5e^{+/-}$ and $Inpp5e^{-/-}$ MEFs expressing 5HT$_6$-mCeru3 and cofilin1-YFP. White arrowhead indicates tip accumulation of cofilin-1.

(E) Relative risk ratio analyses on the effect of differential ciliary PI(4,5)P$_2$ in influencing intraciliary cofilin-1 incidence, as in (D).

(F) Live fluorescence images of NIH/3T3 expressing 5HT$_6$-mCeru3-PIPK or 5HT$_6$-mCeru3-PIPK(KD) and respective YFP-tagged (top) phosphoinositide-binding Kras small GTPase, (middle) Kras tail anchor harboring phosphoinositide-binding module, or (bottom) non-phosphoinositide-binding Hras small GTPase. White arrowheads indicate ciliary localization. While Kras was restricted to the proximal cilia in 5HT$_6$-FP-PIPK(KD)-expressing cells, 5HT$_6$-FP-PIPK expression was sufficient to accumulate Kras into distal cilia. In contrast, Hras accumulated to distal cilia regardless of ciliary PI(4,5)P$_2$.

(G) Quantification of small GTPase or tail anchor accumulation in cilia, expressed as a relative ratio of cilium length, as in (F). Data are represented as mean ± SEM. Two-tailed Student's t tests were performed with respect to each PIPK (KD) condition, p values indicated. (n = 12, 20, 71, 84, 25, 24 cells; 2-3 experiments). Scale bars indicate 1 μm in (A) and 5μm in (B), (D) and (F).
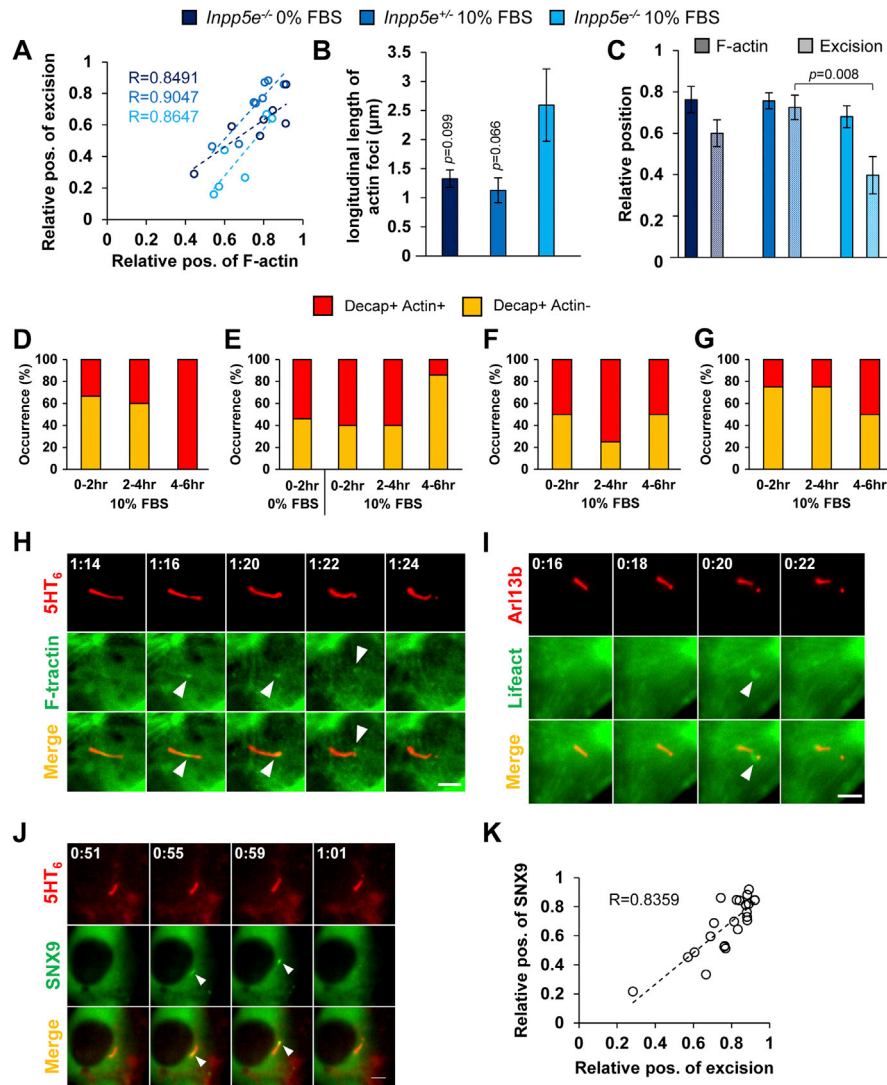
Figure S4. F-Actin and SNX9 Localize in Primary Cilia Prior to Decapitation, Related to Figure 3

(A) Correlation plot of intraciliary F-actin position with excision position, each expressed as relative ratio of cilia length. Color coding as in panel above. Position of F-actin was measured at estimated centroid position of F-actin foci prior to excision. In each case, linear regression is drawn in dashed line, with Pearson correlation coefficient R value indicated. (n = 7, 8, 6 cells from left to right; 2-3 experiments from (D) and (E)).

(B) Quantification of actin foci longitudinal length just prior to excision. Color coding as in panel above. Data shown as mean ± SEM. Student's t tests were performed with respect to $Inpp5e^{-/-}$ 10% FBS condition, p values indicated. (n = 7, 8, 6 cells from left to right; 2-3 experiments from (D) and (E)).

(C) Quantification of relative positions of cilia excision and F-actin. Color coding as in panel above. Data shown as mean ± SEM. Student's t test was performed with p value indicated. (n = 7, 8, 6 cells from left to right; 2-3 experiments from (D) and (E)).

(D) Percentage of cilia decapitation events with or without co-observed intraciliary F-actin in $Inpp5e^{+/-}$ MEFs expressing 5HT$_6$-YFP and mCeru3-Lifeact between 0-2, 2-4 and 4-6 hr of 10% FBS stimulation, related to Figure 3C. Of note, the transient nature of intraciliary F-actin could render inefficient capturing by the two-minute experimental imaging intervals, and a high F-actin marker intensity in the cell body could also limit visualization of specific signals in primary cilia; also applies to (E-G). Color coding as in panel above. (n = 6, 5, 4 cells; 2-3 experiments).

(E) Percentage of cilia decapitation events with or without co-observed intraciliary F-actin in $Inpp5e^{-/-}$ MEF 5HT$_6$-YFP and mCeru3-Lifeact between 0 and 2 hr in 0% FBS, or between 0-2, 2-4 and 4-6 hr of 10% FBS stimulation, related to Figure 3D. Color coding as in panel above. (n = 13, 5, 5, 7 cells; 2-3 experiments).

(F) Percentage of cilia decapitation events with or without co-observed intraciliary F-actin in $Inpp5e^{+/-}$ MEFs expressing 5HT$_6$-mCeru3 and alternative F-actin sensor, F-tractin-Citrine, at respective time periods of 10% FBS stimulation, see (H) below. Color coding as in panel above. (n = 2, 4, 2 cells; 2 experiments).

(G) Percentage of cilia decapitation events with or without co-observed intraciliary F-actin in $Inpp5e^{+/-}$ MEFs expressing Lifeact-mCeru3 and alternative ciliary membrane marker, Arl13b-YFP, at respective time periods of 10% FBS stimulation, see (I) below. Color coding as in panel above. (n = 4, 4, 4 cells; 2 experiments).

(H) Time-lapse images of $Inpp5e^{+/-}$ MEFs expressing 5HT$_6$-mCeru3 and F-tractin-citrine between 0hrs and 2hrs post-stimulation with 10% FBS, as in (F). White arrowheads indicate F-actin assembly at site of cilia excision.

(I) Time-lapse images of $Inpp5e^{+/-}$ MEFs expressing Arl13b-YFP and Lifeact-mCeru3 between 4hrs and 6hrs post-stimulation with 10% FBS, as in (G). White arrowheads indicate F-actin assembly at site of cilia excision.

(legend continued on next page)

(J) Time-lapse images of *Inpp5e*$^{+/-}$ MEFs expressing 5HT$_6$-mCeru3 and YFP-SNX9 between 4hrs and 6hrs post-stimulation with 10% FBS. Arrowheads indicate SNX9 propagation from proximal cilia to distal site of cilia excision.

(K) Correlation plot of SNX9 intraciliary position with position of excision, each expressed as relative ratio of cilia length. Position of SNX9 was measured at estimated centroid position of SNX9 foci just prior to excision. Linear regression is drawn in dashed line with Pearson correlation coefficient R value indicated. (n = 23 cells; 2 experiments).

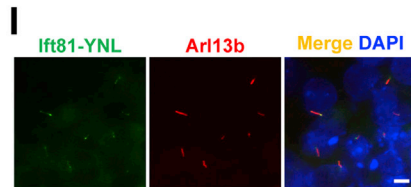Time in hr:min. Scale bars indicate 5μm.
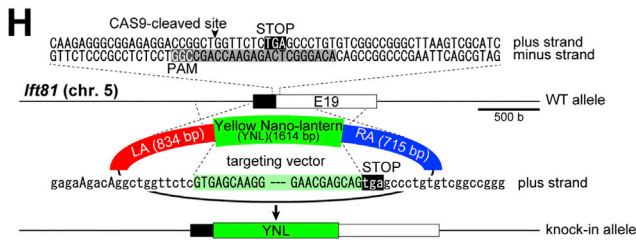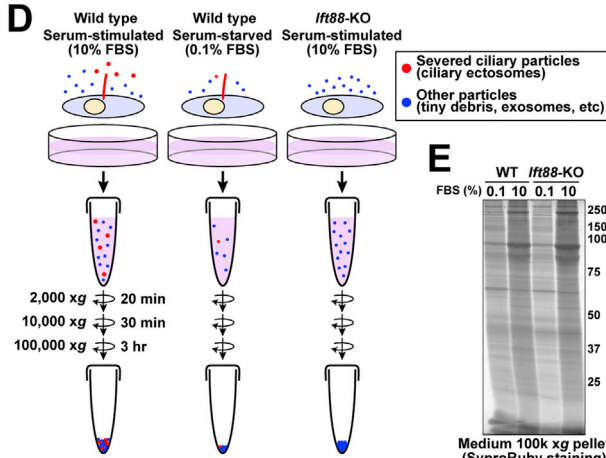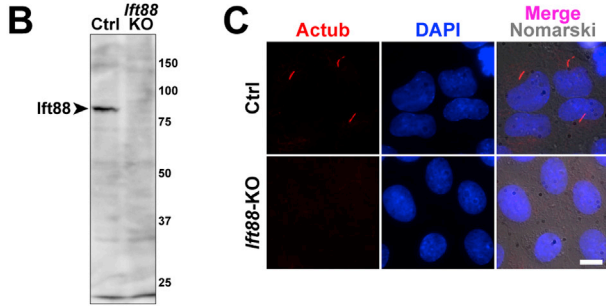
(legend on next page)
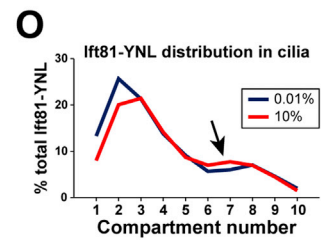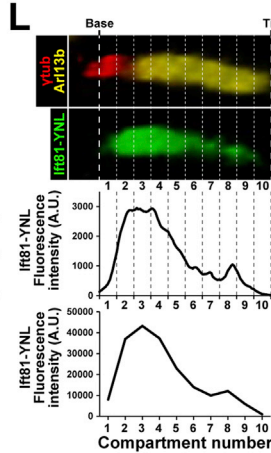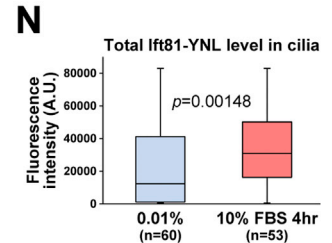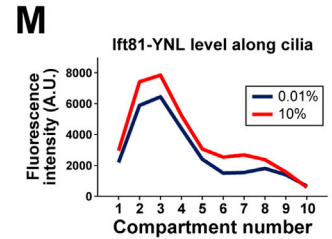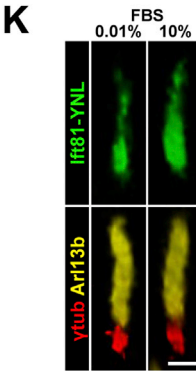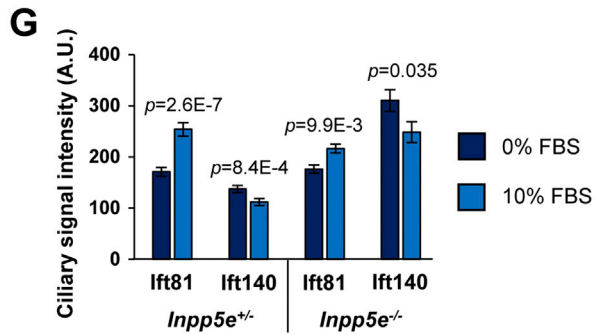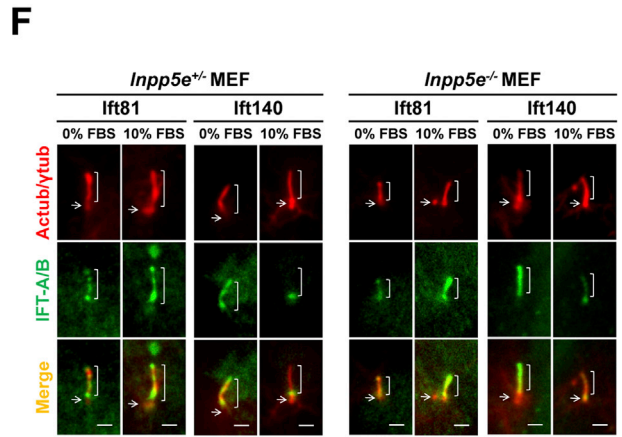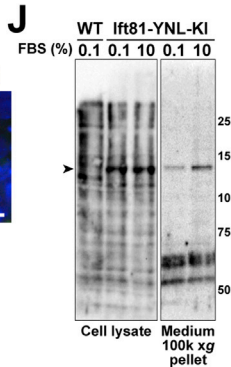
Figure S5. Experimental Scheme for Ciliary Vesicle Proteomic Profiling and Analyses of Ciliary IFT Distribution, Related to Figure 4

(A) Generation of *Ift88*KO mIMCD-3 cell line using CRISPR/CAS9-based genome editing technique. The target sequence of guide-RNA (gRNA) used was placed on the minus strand of the genome corresponding to the exon 3 of *Ift88*. Generated *Ift88*KO mIMCD-3 cell line had bi-allelic frameshift insertion at the CAS9-cleaved site.

(B) Loss of Ift88 expression was verified using western blot analysis with an anti-Ift88 antibody.

(C) Actub immunofluorescence revealed that *Ift88*KO mIMCD-3 cells lack primary cilia.

(D) Schematic illustrating the collection and processing of conditioned culture media under indicated conditions. Culture media were first pelleted at low centrifugal force to remove large cell debris, followed by higher centrifugal forces to concentrate smaller ciliary vesicles and exosomes.

(E) Representative SDS-PAGE of 100k xg pelleted conditioned media under conditions illustrated in (D), as visualized by SyproRuby staining.

(F) Actub/γtub and Ift81/Ift140 immunofluorescence of *Inpp5e$^{+/-}$* and *Inpp5e$^{-/-}$* MEFs treated with 0% FBS or 10% FBS for 4 hr. Images within Ac tub/γtub and Ift81/Ift140 image panels in each column group are scaled to same intensity range. Brackets indicate axoneme, while arrows mark centrosomes.

(G) Signal intensity measurements of Ift81 or Ift140 immunofluorescence in primary cilia (cilia - vicinity background) under indicated conditions, as in (F). Data are represented as mean ± SEM. Two-tailed Student's t tests were performed with respect to each 0% FBS condition, *p* values indicated. (n = 114, 118, 90, 88, 14, 113, 87, 79 cells for respective data from left to right; 3 experiments).

(H) Schematic illustration of yellow Nano-lantern (YNL) knock-in into 3′ end of *Ift81* to generate Ift81:YNL knock-in mIMCD-3 cell line.

(I) Ift81-YNL co-localizes with Arl13b immunofluorescence in Ift81:YNL knock-in mIMCD-3 cell line.

(J) Western blot detection of YNL-tagged endogenous Ift81 (arrowhead) using anti-GFP polyclonal antibody in total cell lysates or particle-enriched 100k-g culture media pellets of WT or Ift81:YNL knock-in mIMCD-3 after a 24 hr stimulation with either 0.1% FBS or 10% FBS.

(K) Fluorescence images of Ift81-YNL with Arl13b and γtub immunofluorescence upon 4 hr 0.01% FBS or 10% FBS stimulation of Ift81:YNL knock-in mIMCD-3.

(L) Schematic illustration of cilia length compartmentalization used for ciliary Ift81 analyses in (M)-(O). For each primary cilium, YNL fluorescence intensities along cilia length was first obtained using a line scan spanning from base to tip of cilium (middle), and total fluorescence intensity within each compartment was derived via signal integration (bottom).

(M) Quantification of mean Ift81-YNL fluorescence intensities along length of primary cilia subjected to 4 hr stimulation with 0.01% FBS or 10% FBS. (n = 60 for 0.01% FBS; n = 53 for 10% FBS).

(N) Quantification of total Ift81-YNL fluorescence signals of primary cilia subjected to 4 hr stimulation of either 0.01% FBS or 10% FBS. Total Ift81-YNL level in each cilium was calculated via integration of fluorescence signals across all compartments described in (L). Data are shown as median ± quartile (box) and 90 percentile (bars). Mann-Whitney U-test was performed with *p* values indicated. (n = 60 for 0.01% FBS; n = 53 for 10% FBS).

(O) Quantification of mean Ift81-YNL fluorescence signal distribution along cilia length, expressed as a percentage of total Ift81-YNL fluorescence signals as in (N).

Scale bars indicate 10 μm in (C), 2 μm in (F), 5 μm in (I) and 1 μm in (K).
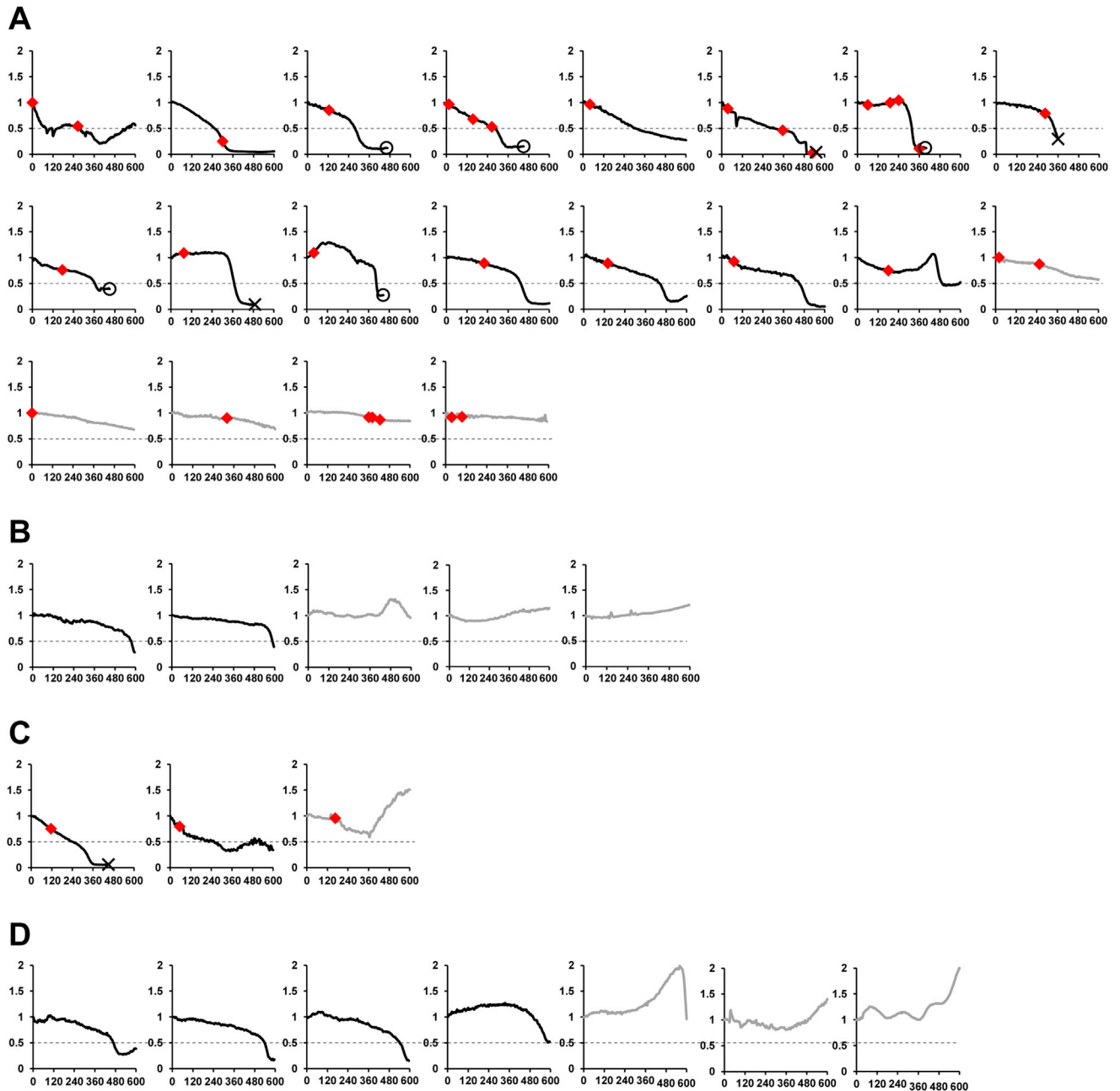
Figure S6. Time-Lapse Measurements of Nuclear Venus-p27K⁻/mCherry-hCdt1(30/120) Signal Intensity Ratios under Growth Stimulation, Related to Figure 6

Time-lapse measurements of nuclear Venus-p27K⁻/mCherry-hCdt1(30/120) signal intensity ratios in:

(A) Decap+ $Inpp5e^{+/-}$ MEFs expressing $5HT_6$-mCeru3;

(B) Decap- $Inpp5e^{+/-}$ MEFs expressing $5HT_6$-mCeru3;

(C) Decap+ $Inpp5e^{+/-}$ MEFs expressing $5HT_6$-mCeru3-Tβ4(WT);

(D) Decap- $Inpp5e^{+/-}$ MEFs expressing $5HT_6$-mCeru3-Tβ4(WT).

Horizontal axes indicate time (min); vertical axes indicate basal normalized ratios of Venus-p27K⁻/mCherry-hCdt1. Black dashed lines indicate arbitrary G_0-G_1 transit mid-point. Red diamonds mark time points of cilia decapitation events. Open circles indicate beginning of mCherry-hCdt1(30/120) signal decrease (signifying start of S-phase transit). Crosses indicate end of imaging period. Responses plotted in gray were cells which maintained ratio values > 0.5 throughout the 10 hr imaging period (these cells did not demonstrate a sharp decrease in Venus-p27K⁻, i.e., not determined for quiescence exit), and were excluded from time measurements in Figure 6E.